Memoirs of the Faculty of Science, Kyoto University, Series of Physics, Astrophysics, Geophysics and Chemistry, Vol. XXXVII, No. 1, Article 1, 1986

Measurement of the Differential Cross Sections of η and η' Produced in $\pi^- p$ Charge Exchange Reactions at 8.06 GeV/c

By

Junpei SHIRAI

Department of Physics, Faculty of Science, Kyoto University Kyoto, 606, Japan

(*Received Feb. 9, 1985; Revised March 8, 1985*)

Abstract

A high statistics measurement of cross sections for $\pi^- p \to \eta n$ and $\pi^- p \to \eta' n$ at 8.06 GeV/c was performed using charged particle and gamma ray spectrometer at the KEK. A total of 14,600 η and 4,500 η' mesons were recorded. The behavior of the differential cross sections for η and η' is different with each other and the ratio $R(\eta'/\eta)$ of the differential cross sections decreases with four-momentum transfer squared $-t$ by a factor of 3 in the region of $|t|<0.8$ GeV^2 and beyond $|t|=1.0$ GeV^2 $R(\eta'/\eta)$ increases and reaches to 1 at $|t|=1.3$ GeV^2. $R(\eta'/\eta)$ at $t=0$ is 0.55 ± 0.04 and $\eta-\eta'$ mixing angle is $-(18.1\pm 1.0)°$ by the simple mass-mixing scheme, which is different from the values from the linear ($-24°$) and quadratic ($-10°$) mass formulae of naive SU(3) classification.

1. Introduction

The comparison between the η and η' mesons production cross sections in the $\pi^- p$ charge exchange reactions has been of great interest from a view point of the quark model (ref. 1). Since the initial $\pi^- p$ system of both reactions.

$$\pi^- p \to \eta n\,, \tag{1}$$

and

$$\pi^- p \to \eta' n\,, \tag{2}$$

does not contain the strange quark (s) content, the η and η' mesons are produced only through the light quark (u and d) contents by the dominant OZI-allowed process. The ratio of the cross sections provides information on the relative non-strange quark content in η nad η'.

According to the SU(3) theory, η and η' are isoscalar members of the pseudoscalar nonet, but the nonet does not satisfy the typical mass formula, and a symmetry-breaking interaction has been introduced to take care of octet-singlet mixing. A general mixing scheme for the $\eta-\eta'$ complex is given by (ref. 2),

$$|\eta> = S_1(\cos\theta_1|\eta^8> - \sin\theta_1|\eta^0>)\,, \tag{3}$$

$$|\eta'> = S_2(\sin\theta_2|\eta^8> + \cos\theta_2|\eta^0>)\,, \tag{4}$$

---

* Now at the Nationale Laboratory for High Energy Physics, Ibaraki-ken, Japan.

where η^8 and η^0 are the octet and singlet isoscalar members of SU(3) nonet whose quark content are defined as follows;

$$|\eta^0> = (uu+dd+ss)/\sqrt{3}\ , \tag{5}$$

$$|\eta^8> = (uu+dd-2ss)/\sqrt{6}\ . \tag{6}$$

This leads the ratio $R(\eta'/\eta)$ of the cross sections of reactions (1) and (2) to be

$$R(\eta'/\eta) = (S_2 \sin(\theta_0+\theta_2)/S_1 \cos(\theta_0+\theta_1))^2\ , \tag{7}$$

with

$$\theta_0 = \tan^{-1}\sqrt{2} = 54.74^\circ\ . \tag{8}$$

If we assume a simple mass-mixing scheme with $S_1=S_2=1$ and $\theta_1=\theta_2=\theta$, $R(\eta'/\eta)$ can be expressed as follows;

$$R(\eta'/\eta) = \tan^2(\theta_0+\theta)\ . \tag{9}$$

The value of the mixing angle θ is determined from the mass of the 0^- nonet to be -24° or -11°, depending on the linear or quadratic SU(3) mass formula, which gives the value of $(R(\eta'/\eta)=0.35$ and 0.96, respectively. Therefore the measurement of $R(\eta'/\eta)$ will give informations on mixing angle and make it possible to determine the mixing angles, and to test the reliability of the simple mass-mixing scheme. In this scheme, $R(\eta'/\eta)$ does not depend on incident momenta and momentum transfer squared.

In order to identify the reactions (1) and (2), 2γ's from η and η' or $\pi^+\pi^-\gamma\gamma$ must be detected, since η and η' decay as follows;

$$\eta \to \gamma\gamma$$
$$\to \pi^+\pi^-\pi^0,\ \pi^0 \to \gamma\gamma$$
$$\eta' \to \gamma\gamma$$
$$\to \pi^+\pi^-\eta,\ \eta \to \gamma\gamma$$

Previous experiments on the reactions (1) and (2) cover a wide momentum range from 3.8 to 200 GeV/c (refs. 3–14). Main features of the experimental results are summarized in table 1. However, all of them except refs. 10 and 14 detected η and/or η' in $\gamma\ \gamma$ decaying mode. The very small size of the branching ratio of η' into $\gamma\gamma$ decay severely limited the data by statistics. In addition, heavy backgrounds occurred from comparatively intense processes of $\pi^-p \to \omega n$ (with $\omega \to \pi^0\gamma$), $\pi^-p \to \pi^0\pi^0 n$, and also $\pi^-p \to f^0 n$ (with $f^0 \to \pi^0\pi^0$) in which some of the gamma rays were undetected or unseparated from others. This caused the systematic error in identifying η' in the $\gamma\gamma$ mass spectrum.

Two recent experiments measured $R(\eta'/\eta)$ with very high-statistics. One of them (ref. 13) detected η and η' via their $\gamma\gamma$ decays at incident momenta from 15 to 40 GeV/c. Their results shows the same s-dependence of the cross sections for the reaction (1) and (2). The t-dependence is also the same for both processes. They obtained the average value of 0.52 ± 0.02 for $R(\eta'/\eta)$ of total ross sections and

Table 1. List of previous experiments for $\pi^-p\to\eta n$ and $\pi^-p\to\eta' n$

Incident momentum (Gev/c)	Particle	Detection	Reference
2.91, 3.72, 5.9, 9.8, 13.3 and 18.2	η	2γ	Guisan et al. (3)
10.0	η	2γ	Wahlig et al. (4)
3.65	η, η'	2γ, n	Harvey et al. (5)
3.8	η'	2γ, n	Apel et al. (6)
3.8,6, 8 and 12	η, η	2γ, n	Apel et al. (7)
21,25, 32.5, 40 and 48	η	2γ	Bolotov et al. (8)
32.5 and 48	η'	2γ	Bolotov et al. (9)
6.0	η	$\pi^+\pi^-\gamma\gamma$	Shaevitz et al. (10)
20.8, 40.8, 64.4, 100.7, 150.2 and 199.3	η	2γ	Dahl et al. (11)
15, 20.2, 25, 30, and 40	η	2γ	Apel et al. (12)
15, 20.2, 25, 30 and 40	η'	2γ	Apel et al. (13)
8.45	η, η'	$\pi^+\pi^-\gamma\gamma$	Stanton et al. (14)

0.55 ± 0.06 for $R(\eta'/\eta)$ at $t=0$. They concluded that the reaction (2) was simply a scaled-down version of reaction (1) and $R(\eta'/\eta)$ did not depend on t. The other high-statistics experiment (ref. 14) was performed at 8.45 GeV/c by detecting $\pi^+\pi^-\gamma\gamma$ with the charged and neutral spectrometer at the Argonne National Laboratory. They obtained the value of 0.48 ± 0.08 for $R(\eta'/\eta)$ at $t=0$ and it decreases strongly with t by a factor of 4 at $|t|<1.0$ GeV^2 in contradiction with the former statements.

These experimental values of about 0.5 for $R(\eta'/\eta)$ at $t=0$ derive the mixing angle of $-19°$ from the simple mass-mixing scheme (9). These experimental results cannot be explained by the simple quark model. Several speculations have been made on the quark content of η'. It was suggested that the wave function of η' might have additional mixing of radially excited states (refs. 15, 16), or η' might contain the gluonium component (ref. 17, 18), which will behave as an inert component in the reaction (2).

It is essential to take the data of clean events with statistics high enough to clarify the t-dependence of $R(\eta'/\eta)$ in more detail over the wide t-range.

The present experiment has been performed at the National Laboratory for High Energy Physics (KEK) from November 1982 to July 1983, using 8 Gev/c π^- beam and a wide acceptance charged particle and gamma ray spectrometer. Our data has the largest sample of reaction (2) at any momentum. The reactions (1) and (2) have been measured through $\pi^+\pi^-\gamma\gamma$ mode and this enabled us to take very clean events of η and η' with small backgrounds due to the high mass resolution. The experimental apparatus and the data analysis are described in Chapters 2 and 3, respectively. In Chapter 4 the results will be given and compared with the previous experimental results and theoretical predictions.

2. Description of the Experimental Apparatus

The apparatus we used was a forward spectrometer (fig. 1). The momenta of

charged particles were measured with a large aperture analyzing magnet "BENKEI" and four sets of multi-wire proportional and drift chambers (W1, W2, W3 and W4). The energy and position of gamma rays were measured with an array of lead glass blocks equipped with active converters and a proportional chamber (W5). The recoil neutron was not detected. The liquid hydrogen target was a 21 cm long and 5 cm in diameter. The pion beam was provided by a high energy beam line (π1) at the National Laboratory for High Energy Phygics (KEK).

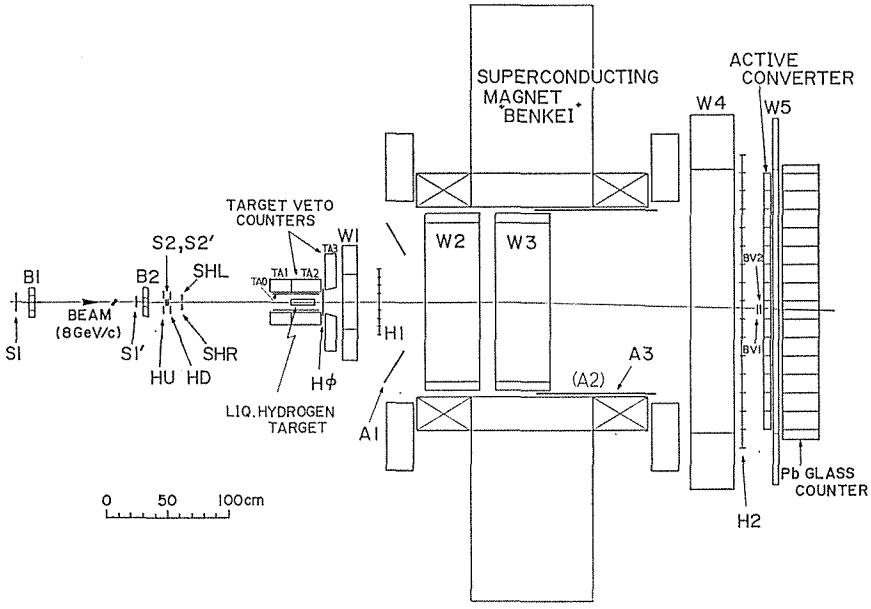

Fig. 1 Experimental layout.

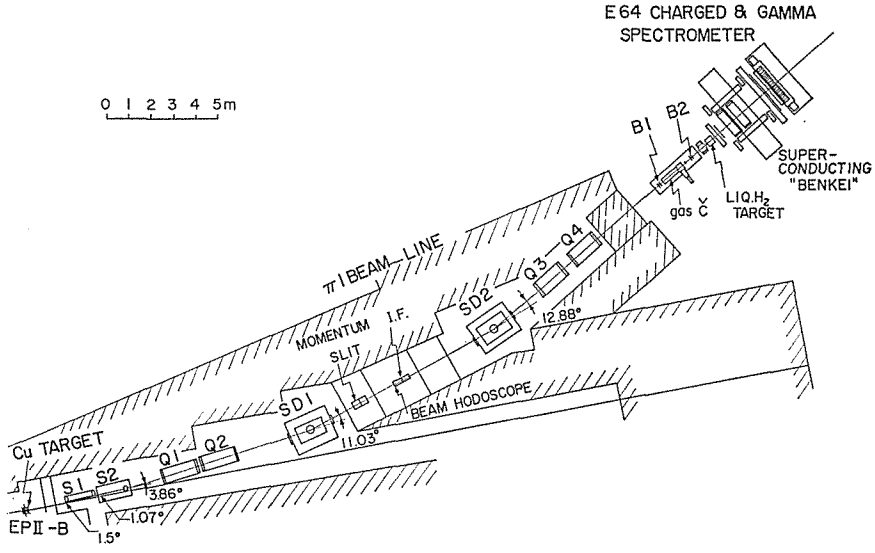

Fig. 2 π1 beam line.

2.1 Beam and Target

Pions were produced in a copper production target of 10 mm in diameter and 60 mm long irradiated with a slowly extracted proton beam (EPII-B) of the 12 GeV proton synchrotron at KEK as is seen in fig. 2.

The particles produced in the angle of 1.5 degree were bent by a pair of septum magnets (S1, S2) and focused with a quadrupole doublet (Q1, W2) onto an adjustable momentum slit having a large momentum-dispersion. A beam hodoscope BH, a series of ten finger scintillation counters was placed at this intermediate focus point. Each element was 6 mm wide and was installed such that one third of the width was overlapped with an adjacent element. Each particle was tagged with a momentum bite of 0.2% at 8 GeV/c.

Two superconducting bending magnets (SD1, SD2) placed before and behind the intermediate focus point deflected the beam against the primary proton line by 23.91 degrees. A second quadrupole doublet (Q3, Q4) refocused the beam onto the hydrogen target which was placed at 35 meters downstream from the production target.

The beam size at the hydrogen target was 30 millimeters in diameter. The divergence of the beam was ± 12 mrad. The typical beam intensity was 1.1×10^5 particles per burst with a momentum bite of 1.2% at a rate of 8×10^{11} protons per burst on the production target. The beam spill was 400 msec long in every 2.5 sec. The effective beam intensity through a beam defining counter telescope was 8×10^4 particles per burst.

Two sets of beam proportional chambers, B1 and B2, were placed 3.25 m and 1.25 m upstream of the target center, respectively. Each set consisted of x and y planes and the wire spacing was 2 mm for B1 and 1 mm for B2. The directions of the incident particles were measured with accuracies of ± 0.8 mrad.

The number of particle contaminants were measured at several momenta with a gas Cerenkov counter (containing Freon13) placed between B1 and B2, and with the time-of-flight between intermediate and final focus points. The slit sizes of collimaters were 12.5 mm. The muon contamination was measured to be 2.8 ± 0.2% at the momentum of 8 GeV/c. The contaminants of Kaons, anti-protons, and electrons were negligiblly small at this momentum. The decay fraction of pion between the last bending magnet (SD2) and the final focus point was estimated to be 2.9% and agreed with the measured muon contamination.

Liquid hydrogen was filled in a cylindrical mylar box (appendix) of 21 cm long and 5 cm in diameter. The mylar thickness wsa 0.2 mm. The hydrogen gas filled in a reservoir tank (2 m^3) was transmitted to the condenser via a liquid nitrogen purifier. The gas was liquefied in the condenser and gathered in the appendix. The level of the liquid hydrogen in the appendix was monitored throughout the experiment by small carbon resistors placed in the top and bottom of the appendix. By closing a cryo-valve, liquid hydrogen in the appendix was easily pushed back to the condenser. Thus the appendix was made empty within a few minutes.

2.2 General Features of the Spectrometer system

The spectrometer system had the following features;

a) wide acceptance in the detection of the decaying particles.
b) good momentum resolution for charged particles.
c) good energy and position resolution for gamma rays.
d) high tracking efficiency.
e) good trigger efficiency.
f) efficient data taking system.

In order to provide a wide geometrical acceptance the detectors were closely assembled in and around the analyizng magnet. The distance between the hydrogen target and the lead glass wall was 4 meters and a solid angle of the spectrometer acceptance was 0.2 steradian. An anticounter system was installed around the target and inside the magnet in order to suppress unwanted background reactions. The anticounter system was sensitive to both charged particles and gamma rays, and covered more than 90% of the forward off-spectrometer region.

2.3 Spectrometer Magnet

The spectrometer magnet was a large window frame type superconducting magnet called "BENKEI" (ref. 19). Its center was placed 188 cm downstream from the hydrogen target. The effective field volume was 1.0 meter heigh, 1.5 meter wide, and 2.2 meter long. In order to detect charged particles with low momenta (>350 MeV/c), the operational current was set at 300 A, which was far below the rating current of 600 A. The central field and the field integral were 8.4 kilogauss and 12.4 kilogauss-m, respectively.

The magnetic field was measured over the 8000 points in one-eighth of the symmetric volume. The asymmetry was measured to be at most 150 gauss and the field integral was constant within 5.7% over the aperture. The magnetic field at each measured z-position was fitted by a set of five-dimensional polynomyals of x and y coordinates. The magnetic field at any z-position was derived by interpolating the coefficients from the neighbouring z-points of the measurement.

A large refrigeration system of helium was prepared for the beam line magnets of superconducting septum (S2) and two dipole magnet (SD1, SD2) and for the superconducting BENKEI. The system was successfully operated throughout the experiment.

2.4 Tracking Chambers

2.4.1 General Features

The trajectories of the secondary charged particles through the reaction were measured by four sets of stacked chambers W1, W2, W3 and W4. Each set consisted of two multiwire proportional chambers (MWPC-x,y) and two pairs of drift chambers (xx' and yy'). The characteristics of the chambers are summarized in table 2.

Table 2 Chamber characteristics

Chamber set	Number and type in set	Sensitive area (cm)	Anode wire spacing (mm)	Readout
B1	2 MWPC	12.8×12.8	2	
B2	2 MWPC	6.4×6.4	1	
W1	2 MWPC 4 DC	48×32	2 10	2-dim, (one of X and Y)
W2	2 MWPC 4 DC	128×76	2 21	2-dim, (one of Y)
W3	2 MWPC 4 DC	128×76	2 21	2-dim, (one of Y)
W4	2 MWPC 4 DC	215×150	3 50	2-dim, (one of X)
W5	1 MWPC	215×150	3 (5 mm spacing of U, V strips)	Both anode (Y) and cathode (U, V) readout

The stacked chamber system has several advantages; The chambers were closely assembled to each other. The chambers were aligned easily with high accuracy. The chamber materials were reduced to suppress the reactions and multiple scattering of the secondary particles. From a view point of analysis, the direction of the charged particle track was derived in each chamber set and the efficient track finding was performed.

The proportional chambers were used for efficient triggering and track finding. The wire configuration of drift chambers in xx' and yy' pair was staggered each other by a half cell size. This wire configuration, combined with the information of the proportional chmabers was useful to resolve the left-right ambiguity with ease. Five drift chambers (one of the x-drift chambers of W1 and W4, and one of the y-drift chambers of W1, W2, and W3) were equipped with two-dimensional readout system of the charge division. The stereo-ambiguity in multi-charged events were eliminated by making use of the information of these chambers.

2.4.2 Structure

The epoxyglass frames and mylar windows were used for W1, W2 and W3. W2 and W3 had the same structure. Fig. 3 shows the structure and the wire configuration of W2, respectively. The stacked system enabled us to reduce the chamber material as mentioned. For W1, W2 and W3 the amount of material per plane was only 20 mg/cm^2 (0.001 radiation lengths). The wire spacings are also listed in table 2. The small cell size of the drift chambers reduced the events with more than one charged particle passing through the one drift cell. The electric field of the drift chambers was given by the cathode wires at increasing potentials. The anode wires of W1, W2 and W3 were gold-plated tungsten of 20 μm in diameter. The cathode wires were copper-beryllium wires of 50 μm in diameter.

W4 was the largest chamber set in the system with .2.15×1.5 m^2 effective area. It was made of acrylic foam boards with epoxyglass frames. The anode wires were 30 μm in diameter of gold-plated tungsten. The cathode plane of MWPC's were

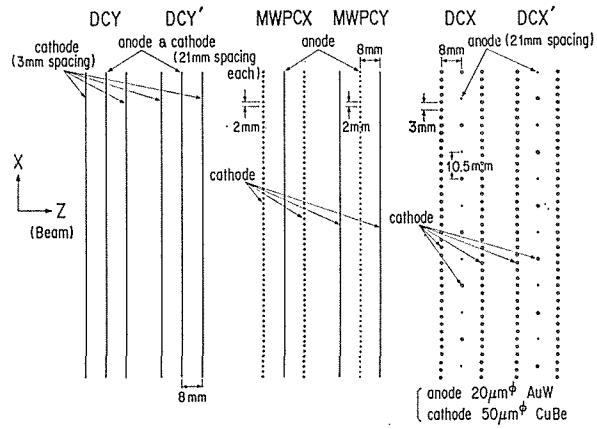

Fig. 3 Wire configuration of chamber set (W2)

aluminum sheets of 100 μm thick glued on the acrylic foam boards. The field shaping cathodes of drift chambers were given by kapton sheets with copper strips of 1 mm wide and 5 mm spacing, which were also glued on the acrylic foam boards. The chamber material of W4 was 420 mg/cm^2 (0.012 radiation lengths) per plane.

2.4.3 Gas Mixture

Fig. 10 shows a gas supply system of the chambers. The gas in the MWPC's was the magic gas, that is, a mixture of argon, isobutane and freon. Methyral was also mixed in order to suppress carbonization of isobutane (ref. 20). Typical mixing ratios were 72% of argon, 25.4% of isobutane, 2.3% of methyral and 0.33% of freon. The ratio of freon was determined by the mean free path for electron capture, λ, which is given by an equation (ref. 21),

$$\lambda = 1/1.5p \text{ mm}, \tag{10}$$

where p is the percentage of freon. The value of p was set so that λ was comparable to the wire spacing. For MWPC's in W4 the content of freon was 0.2% because of laregr wire spacing than the other MWPC's. Liquid methyral was kept in a bottle at constant temperature of 0°C, so that the content of methyral was controlled by the saturated vapor pressure and a flow rate of the argon gas bubbling through the bottle.

The rate of avalanches per single anode wire was higher in the drift chamber than that in the proportional chamber. The decrease in the pulse height by space charge and the carbonization around the anode wires were severer for reliable operation of drift chambers than for proportional chambers. The quenching gas with smaller molecular weight was preferable for drift chambers. A mixture of 60% of argon, 40% of ethane was used for all drift chambers.

Operational tests showed that the drift velocity reached a constant value of 50 μm/nsec at the electric field of 1.2 kV/cm and the velocity did not depend on the mixing ratio when the content of ethane was more than 30%.

The spatial resolutions were measured at three different positions in a drift cell and with different gas mixtures and found to be 240 μm to 590 μm (FWHM) depending on the positions. No clear dependence on the mixing ratio was seen at all positions.

From these test experiments, the gas mixture for drift chambers was fixed to 60% for argon and 40% for ethane. In the present experiment 1.2% of methyral was mixed to the drift chamber gas to extend the plateu of the high voltage curve and to further stabilize the operation. The drift velocity and efficiency were not changed under the additional gas mixture of methyral.

2.4.4 Chambers in Magnet (W2, W3)

W2 and W3 were placed in the analyzing magnet. In order to achieve good linearity and efficiency, a special care was taken to the x- and x'-drift chambers, because the wires were stretched in parallel to the main component of the magnetic field (refs. 22 and 23).

The electric field was tilted so that it canceled out the effect of the magnetic field (ref. 24). Fig. 4 shows the calculated equipotential contours of the x-drift chamber in W3. Figs. 5 and 6 show the measured time spectrum and spacetime relationship for the x-drift chamber in W3. The magnetic field was 8.4 kilogauss. The linearity was good over the full drift region, though the drift velocity was about 20% smaller than that of y-drift chamber. The measured efficiency was greater than 98%. No decrease in local efficiency was seen. However, in fig. 5 a small bump of time spectrum is seen between 60 and 70 counts, which wsa not seen in the time spectrum of y-drift chambers.

The space-time relationship and efficiency were examined by simulation and the results showed that some of the electrons generated just beyond the field wire do not obtain the normal drift velocity due to the weak electric field and make a bump in the time spectrum. However, due to the tilted electric field, major part of electrons around the field wire drift into the adjacent cell and moved to the anode

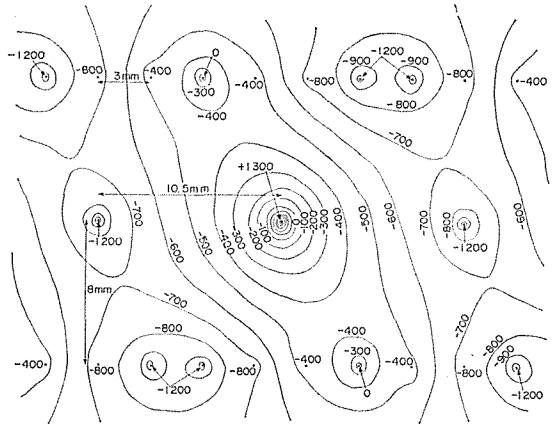

Fig. 4 Equipotential contours calculated for X-drift chamber in W3.

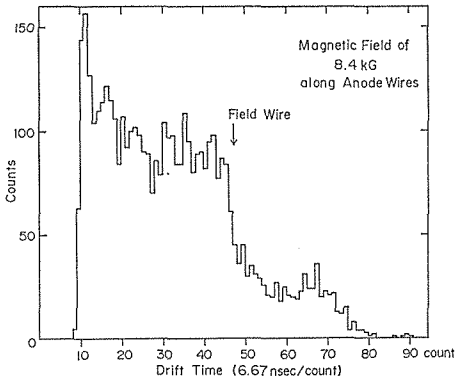

Fig. 5 Time spectrum of X-drift chamber in magnetic field.

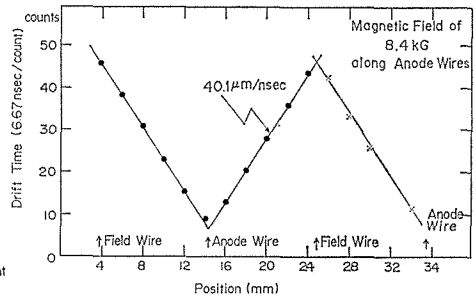

Fig. 6 Linearity of X-drift chamber in W3 in magnetic field. The solid lines are fit by eye.

wire with normal drift velocity. Consequently, the drift time was measured correctly by one of the adjacent anode wires. The simulation also showed that if the electric field was not tilted the efficiency drop was greater than 15%. The estimated inefficiency under the tilted electric field was only 2.3%, which was quite consistent with the measurement. The spatial resolution was measured to be 500 μm (FWHM) in the same magnetic field. The characteristics of y-drift chambers were not influenced with the magnetic field.

2.4.5 Two-Dimensional Readout Method

In order to eliminate the stereo-ambiguity caused by the events with more than one charged track, five drift chambers listed in the table 2 were equipped with the two-dimensional readout system of charge division type. The signals were taken out from both ends of the wires. We call these chambers "two-dimensional" drift chambers to discriminate them from the "one-dimensional" drift chambers measuring the drift time only.

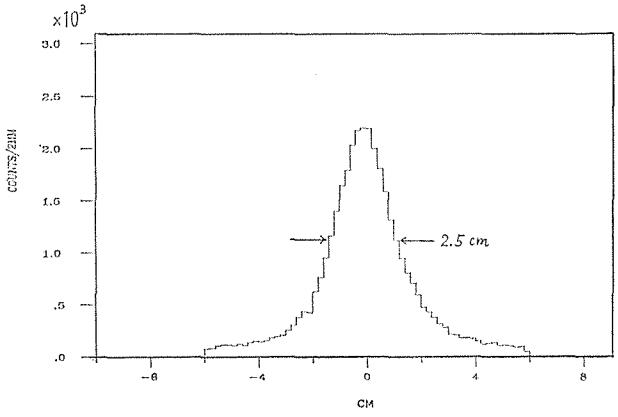

Fig. 7 Spatial resolution of charge division readout (Y-drift chamber in W2).

Nichrome wires of 22 μm in diameter were used for these chambers. The wire resistance is 800 ohms/m. The longitudinal position of an avalanche was determined by the ratio of the charge quantities.

During the experiment the resolution was found to be 1.5% to 4% of wire lengths depending on the chambers. Fig. 7 shows the difference between x-positions of the charged particles measured by the y-drift chamber in W2 and those determined by reconstruction procedure. The lower spatial resolution was partially caused by the attenuation of the signal transmitting the long anode wires compared with the test chamber, and partially caused by the lower S/N ratio than in the test experiment. But it was good enough to resolve the stereo-ambiguity in the reconstruction procedure.

2.4.6 Read-out Method and Electronics for Chambers

a) Signal Readout

In W1 and W4 preamplifiers were mounted on the chamber frames. The amplification factor was set higher for drift chambers than for MWPC's to reduce the time slewing. Low input impedance preamplifiers (50 ohms) were used for two-dimensional drift chambers.

In order to provide a wide geometrical acceptance, the effective area of W2 and W3 should be as large as possible in the limitted space of the magnet. Therefore, the chamber signals were sent out by 5 m-long flat calbes to the preamplifier stations outside of the magnet. The cable consists of 20 pairs of signal and ground lines and the characteristic impedance is 50 ohms. The level of the induced signal of this cable was found to be –24 dB per meter, and this resulted that the amount of cross-talk signals of a typical chamber set was less than 1% of that of the real signals.

Due to the large capacitance (300 pF) of the long microstrip line, chamber signals would be distorted. It was especially severe for the drift chamber, because it worsens the time resolution. To suppress the effect and reduce the time slewing, the input impedances of preamplifiers of W2 and W3 were chosen to match with the characteristic impedance of the microstrip line.

Output signals from preamplifiers were sent to the counting room through 16-pair twisted cables of 30 m long for all proportional chambers and "one-dimensional" drift chambers. Coaxial cables (50 ohms in characteristic impedence) of 90 m long were used for "two-dimensional" drift chambers.

b) Memory Modules for MWPC

The signals from MWPC's were sent to the memory modules built in a CAMAC standard module with double widths. The module accepts 64 signals in parallel through two connectors of 32-plet input. A strobe signal from NIM logics opened the input gate. The width of the strobe signal was clipped to 80 nsec by a fixed delay line, so as to reject the background signals. The module also had two 64-plet output connectors. The chamber signals thus shaped were transmitted to the other modules such as trigger logic modules in the fast selective trigger system (sec. 2–8).

c) Readout Modulaes of Drift Chambers

Two kinds of readout electronics modules were used for drift chambers. They were drift time digitizers (DTD's), and time and amplitude digitizers (TAD's).

DTD's used to measure drift time for "one-dimensional" drift chambers were built in a CAMAC single width module and have 16 channels per module. The chamber signals were internally delayed by 300 nsec and formed the stop signals for DTD. The DTD module started to count the clock signals immediately after the start signal generated by the strobe signal. The clock signals generated by a single clock generator were sent to all DTD's through clock fanout modules. The clock signals having the time duration of 600 nsec were triggered by the start signal.

The spatial resolution of three identical drift chambers was measured as a function of the frequencies of the clock signal. Fig. 8 shows the results. The spatial resolution was almost constant above 100 MHz. At the frequency of 100 MHz the spatial resolution reached 500 μm (FWHM), which was comparable to the resolution measured with a TDC of time expansion type (LeCroy 2228A). The frequency was fixed to 150 MHz in our experiment.

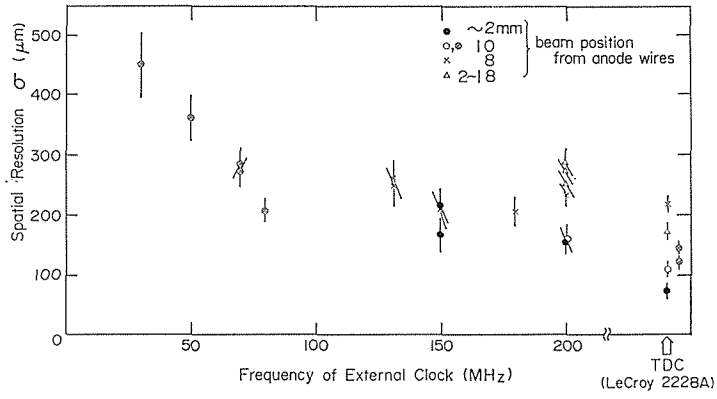

Fig. 8 Spatial resolution of drift chamber as a function of clock frequency.

TAD's used to measure the pulse height of the signal as well as the drift time for the "two-dimensional" drift chambers were built in a CAMAC single width having 8 channels per module. Each channel accepts four left-right pairs of signals from the drift chambers. When a ready signal was accepted from NIM logics, TAD became ready for a constant time duration. The chamber signal was used as a start signal for TAD. If one of the input pair signals exceeded the threshold level, the module became operational during the time period from the start to the end of ready mode, and constant current flowed into a capacitor. In addition to this, the charges of input pair signals were accumulated in another pair of capacitors. The amount of the charge in the capacitors were digitized with a 12-bit ADC through analogue-multiplexers.

2.5 Gamma Ray Detectors

The pictorial view of the gamma detector system is shown in fig. 9. The system

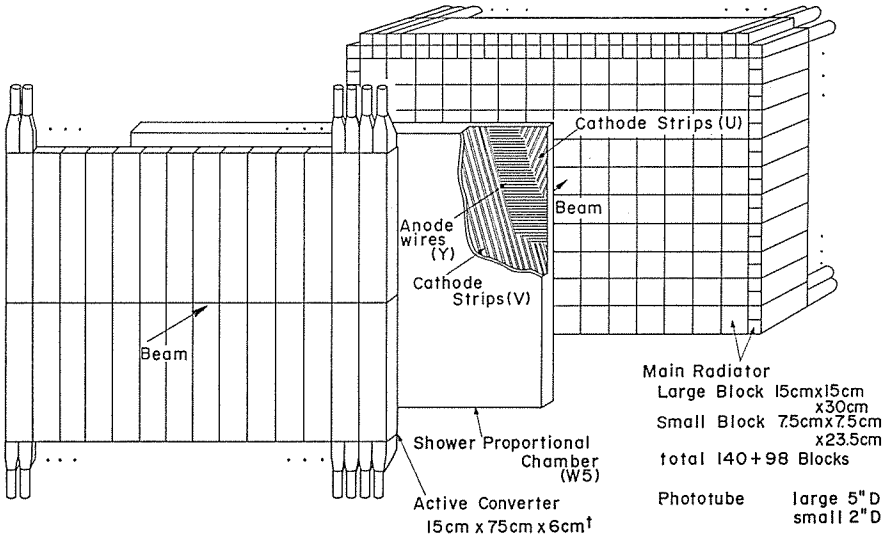

Fig. 9 Gammadetector system.

is composed of lead glass converters (active converters) and a multi-wire proportional chamber W5 followed by total absorption lead glass Cerenkov counters (main radiator).

The main radiator consisted of 238 lead glass blocks and the upstream face was at 397 cm downstream of the hydrogen target and at 7 cm downstream of W5. In the $\pi^+\pi^-\eta$ mode, the maximum momentum of η exceeded 6.5 GeV/c and the energy of gamma ray reached 5.5 GeV. The lead glass blocks must be thick enough to absorb such high energy gamma rays. In addition, the granularity of the blocks must be fine enough to detect separately two gamma rays from neutral pions.

The central part of the main radiator was a 10×14 array of large blocks. The type of the lead glass was SF-5, whose characteristics are presented in table 3. The dimension of a block was 15×15 cm^2 on the face and 30 cm long (11.8 radiation lengths). A 5″-diameter phototube (HAMAMATSU R1250) was directly glued on its downstream face.

The central part was surrounded by 98 blocks of lead glass made of SF-6 to increase the acceptance for the gamma ray. Each block was 7.5×7.5 cm^2 in face and 23.5 cm long (13.1 radiation length). The performance of these blocks are described in refs. 25 and 26. We estimated the effective acceptance of the main radiator including the central and surrounding parts. The effective acceptance is

Table 3. Technical data of dlea glass (SF-5)

Refractive index	1.6737
Radiation length	2.54 cm
Density	4.075 g/cm^3
Transmission at 400 nm wave length	0.991/cm

defined as the detection area where 90% of the energy is absorbed. The effective acceptance of the main radiator was estimated with "EGS III" code (ref. 27) and found to be almost equal to the geometrical acceptance of the central part of the 10×14 array.

The signal from each block was divided into two signals. One of them was digitized by ADC and written onto magnetic tapes. The other signals were sent to the fast logics for event trigger (sec. 2–7).

To achieve the simultaneous optimization of both energy and position resolutions of gamma ray showers, 2×14 array lead glass Cerenkov counters were placed in front of W5 and used as active converters (ref. 28).

Each element of the active converter of the present experiment was 6 cm thick (2.36 radiation lengths), 15 cm wide and 75 cm long. Each element was viewed from one side by two 2″-diameter phototubes through acrylic light guides. The outputs of the two phototubes were linearly added and digitized by ADC's.

W5 was used to measure the position of each gamma ray by detecting the electron showers generated in the active converter. It was placed 390 cm downstream of the hydrogen target and installed immediately downstream of the active converters. The distance between the downstream face of the active converter and the anode plane of the chamber was 1.8 cm. This chamber had the active area of 2.2×1.5 m^2 and was made of acrylic foam boards and epoxyglass frames. The gap between the anode and cathode planes was 8 mm. The anode wires were gold-plated tungsten wires of 30 μm in diameter and were stretched in 3 mm spacing. They were stretched in the horizontal direction. The cathode plane was made of kapton sheets on which the copper strips of 3.5 mm in width were printed with 1.5 mm spacing. The direction of the strips was inclined by ± 60 degrees with respect to the anode wires to give u- and v-coordinates. The x- and y-coordinates of each shower were derived from the induced signals of cathode electrodes as well as those of anode wires. The chamber with a single layer of this type allowed us to obtain the two-dimensional position information at the same z-position (at a position of anode plane) without stereo-ambiguity. The position resolutions were basically equal between x- and y-coordinates. The stereo-ambiguity in multi-shower events was resolved with the three position informations of u-, v- and y-coordinates.

All the phototubes were tightly shielded against the stray field of the analysing magnet. A light pulse from a nitrogen laser system was transmitted to each block through a bundle of thin optical fibers for the monitoring. One of the fibers was connected to the reference phototube which was kept at constant temperature. In order to compensate the drift of the light outputs of the nitrogen laser system, pulse heights of all phototubes were normalized by those of the reference phototube.

In addition to the laser system, a small button of NaI scintillator with an Am^{241} alpha source (ref. 29) was glued onto the corner of the downstream face of each lead glass block. A light output from NaI was recorded at the beginning and the end of every other week running cycle. The data were used to check the gain drifts over a long period of time.

2.6 Anticounter System

In order to suppress many unwanted events and to increase the signal to background ratio, several anticounters were installed, and are listed in table 4 with other trigger counters.

To reject non-interacting beam particles, a pair of beam anticounters BV1 and BV2 were placed at 3.8 m downstream from the target. Each of counters was viewed by two phototubes from top or bottom. The coincidence signals (BV1·BV2) were used to eliminate the Cerenkov signals from the acrylic light guides of these counters.

Three anticounters A1, A2, and A3 were installed inside of the analysing magnet as shown in fig. 1. All of them were constructed with a combination of lead sheets and plastic scintillators so as to be sensitive to both charged particles and gamma rays. They roughly defined the geometrical acceptance of the spectrometer system. A set of picture frame anticounter A1 was used to reject the particles emerging outside of the acceptance of the spectrometer. This counter had two symmetrical sets of element and was mounted just behind the counter hodoscope H1. Each element had four layers of 6 mm thick prastic scintillator interspersed with three layers of

Table 4. List of scintillation counters

Counter	Size (cm)	Layers of scintillator	Position from target center (cm)	Layers of lead (thick. per layer)	Purpose and features
S1	15×15×0.2	1	−341		detect beam
S1′	8× 8×0.2	1	−142		
S2	4× 3×1	1	−111		define start time for trigger
S2′	5× 4×0.1	1	−109		reject N-gamma reaction in S2
HU	15×15×0.6	1	−112	1 (0.2)	reject reactionsin in S2 or other counter materials, with 4 cmϕ hole
HD	15×15×0.6	1	−104	1 (0.2)	
SHL/R	10×10×0.2	2	−96		define beam size with 2.4ϕ cm hole
TA0	0.6 t	1	around the target		reject charged particles and/or gamma rays at wide angles from target
TA1	0.6 t	6		5 (0.4)	
TA2	0.6 t	6		5 (0.4)	
TA3	0.6 t	6		6 (0.4)	
H0	24×15×0.2	1	16		signals forward going charged particles from target
H1	7×15×0.2	1	72		charged particle hodoscope with 8×2 array of elements
H2	15×140×1	1	373		charged particle hodoscope with 16 elements
A1	0.6 t	4	inside the magnet	3 (0.4)	reject particles outside of fiducial
A2	0.6 t	4		3 (0.4)	
A3	0.6 t	2		1 (0.2)	
BV1	10×12×0.6	1	380		reject non-interacting beam particles
BV2	10×12×0.6	1	380		

4 mm thick lead and was covered by stainless steel sheet of 4 mm thick.

Two sets of anticounters A2 and A3 served to reject charged particles not passing through the magnet and gamma rays outside the acceptance. A2 defined the vertical acceptance (± 11 degrees). It had four layers of 6 mm thick of scintillator and three layers of 4 mm thick lead sheets. A3 consisted of two 6 mm thick scintillators and 2 mm thick lead sheets between them. This counter was used to reject low momentum charged particles (less than 350 MeV/c) and gamma rays with large horizontal angles (beyond ± 14 degrees). The light outputs of scintillators in A2 and A3 were transmitted separately through wavelength shifter bars.

The hydrogen target was surrounded by target anticounters TA0, TA1, TA2 and TA3 as shown in fig. 1. They were used to reject large angle charged particles and gamma rays. However, they were insensitive to recoil neutrons.

TA0 was the innermost layer and consisted of 12 scintillation counters. As shown in fig. 10, the width of the counter was chosen so that any of the elements substanded the same solid angle.

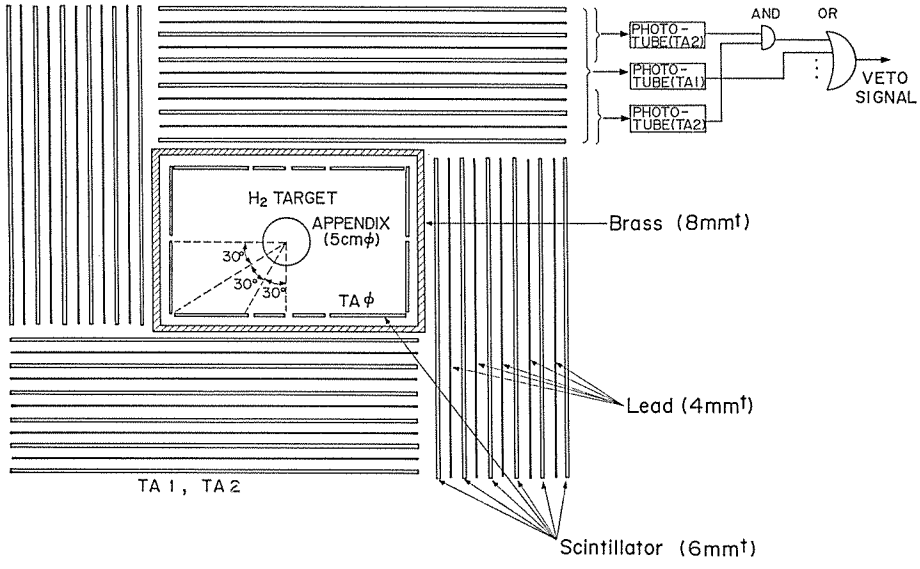

Fig. 10 Target anticounters (TA0, TA1, TA2).

TA1 and TA2 were sandwitch counters having six layers of scintillatiors and five layers of 4 mm thick lead sheets. These counters were located outside of TA0. TA3 was a sandwitch counter having twelve alternating layers of scintillators and 4 mm thick lead sheets. Each of TA1 and TA3 was viewed by 4 phototubes. They were used to reject the background events when any one of phototubes gave a signal.

Each of TA2 was viewed by a pair of phototubes. Each phototube received the lights from inner or outer three layers of scintillators. This counter produced the veto signal if there was at least one pair of signal. This method was effective to suppress overvetoing recoil neutrons.

2.7 Counters and Trigger Logic

The trigger scintillation counters were listed in table 4. These counter signals were combined to give several kinds of trigger signals as shown in table 5. The trigger system enabled us to record not only the required events of two charged particles and two gamma rays ((2C2G" events) simultaneously but also multi-gamma events without charged particles ("N-gamma" events) and other kinds of events for detector calibration and correction.

The incident beam signal was defined by a set of the scintillation counters S1, S1′, S2, S2′ and hole anticounters HU, HD, SHL and SHR. The positions of these counters are shown in fig. 1. S1 and S1′ were wide enough to cover the active area of beam chambers and to monitor the beam halo. S2 was 1 cm thick and was used to define the start time of trigger logic.

S2′, HU and HD were mounted in order to suppress the background reactions in the materials other than the liquid hydrogen target. A thin counter S2′ was placed immediately downstream of S2. It was used to reject reactions with no charged particles in S2. Two 4-cm hole anticounters HU and HD having a 2 mm thick lead sheet were placed before and behind S2 and S2′. They were used to reject charged particles and gamma rays from S2 and other counter materials. The signal from S2 was fed into a discriminator having two kinds of threshold levels. Anticoincidence of the signal above the higher level suppressed the background trigger due to the reactions of multi-charge production in S2. For a "2C2G" event a reaction point was determined with a sufficient spatial resolution from the charged

Table 5. List of trigger mode

Mode	H0 & count down*	H1	H2	Gamma	Veto	Typical event ratio (%)
2C2G#1	CICO#1	H1>1	4>H2>1	NG>1	$\overline{(TG+TC)}$	37
2C2G#2	CICO#2	H1>1	H2>1	NG>1	/	15
2C#1	CICO#2	H1>1	4>H2>1	/	$\overline{(TG+TC)}$	8
2C#2	CICO#3	H1>1	H2>1	/	/	9
2C#3	CICO#3	H1>1	H2>1	/	$\overline{TG}$	5
RAMOFF	CICO#3	H1>1	4>H2>1	/	$\overline{(TG+TC)}$	4
Elastic	CICO#4	H1=1	H2=1	/	TC=1	2
N-GAMMA#1	CICO#1			EG>3 (GeV)	$\overline{(TG+TC+H1+H2)}$	13
N-GAMMA#2	CINO#2			EG>3 (GeV)	$\overline{H1+H2}$	4
$K0_s$	CINO#1	H1≥1	H2>1	/	/	3

* Definition

CICO=BEAM*ANTI*H0

CINO=BEMAM*ANTI*$\overline{H0}$

BEAM=S1*21*S1′*S2*S2′*($\overline{SHL+SHR+HU+HD+S2\ HIGH}$)

ANTI=$\overline{BV1*BV2}+(\overline{A1+A2+A3})$

#1, 2, 3, 4=order of count down

TG=TA1+TA2+TA3

TC=TA0 NG=number of possible gamma rays

EG=total pulse height of lead glass counters

particle tracks. The counter system mentioned above reduced the ratio of the "N-gamma" triggers for empty-target over full-target runs to 0.1.

The charged particles from the target were defined by three scintillation counters H0, H1 and H2. H0 was placed 16 cm downstream of the target center and defined the outgoing charged particles from the target. It also selected "N-gamma" events and "K^0s" eevnts. H1 was a 8×2 array of hodoscope, which was placed in front of the analyzing magnet. The presence of at least two signals from H1 was required in the "2C2G" trigger mode. H2 was a hodoscope consisting of sixteen counter elements. Taking into account the knock-on electrons from upstream materials, double or triple signals were required. Each element was 140 cm long, 15 cm wide, and 1 cm thick. Two phototubes were placed on each side (up and down) of the scintillator. In order to compensate the time slewing due to the amplitude difference, the discriminator of constant-fraction-type was used for each channel. The time differences between the master trigger (defined by S2 counter) and up/down signals were also recorded. The time difference between up and down gave the vertical position along each hit element. It was useful to eliminate the signals stereo-ambiguity of multi-track events with high efficiency.

The time information was also used for the particle identification. A typical momentum versus mass squared plot of the "2C2G" events is shown in fig. 11. In addition to a large number of pion signals, proton and kaon signals are also seen. The events with protons and kaons which were identified apparently were rejected to clarify the $\pi^-p\to\pi^+\pi^-\gamma\gamma n$ reactions.

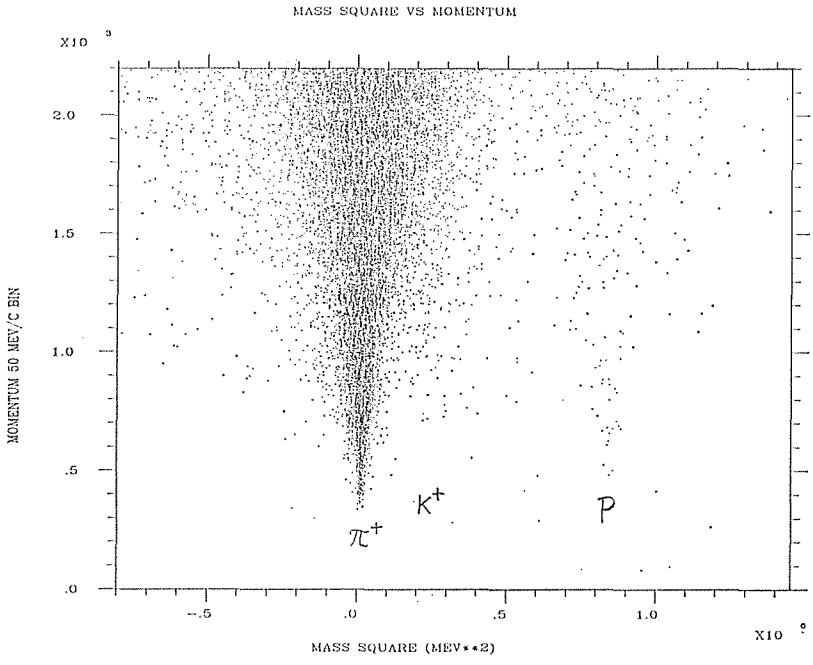

Fig. 11 Momentum versus mass squared for secondary charged particles.

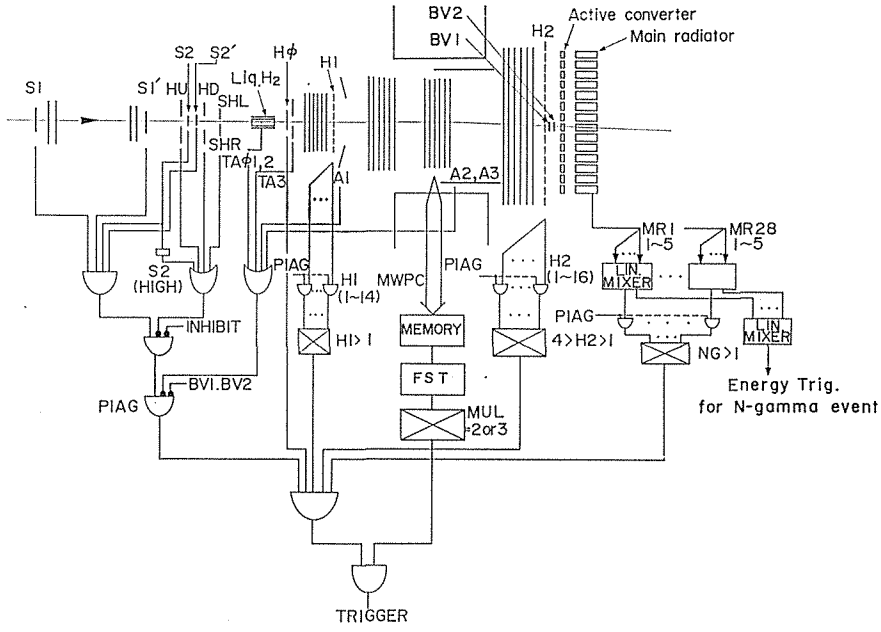

Fig. 12 Simplified tigger diagram.

The main radiator signals fed to the trigger logics were linearly summed and grouped to twenty eight blocks according to the geometrical setup of the active converter elements. The discrimination level was set at 300 MeV. The logic signals passing the discriminators were sent to the multiplicity logic module. More-than-one such signals were reuqired for "2C2G" event trigger. On the other hand, all the signals of the main radiator were summed up for "N-gamma" trigger. The summed signals were then used to select the event of which the energy deposit of all gamma rays were more than 3 GeV.

A simplified diagram of the fast trigger logics is shown in fig. 12. The conditions for the "2C2G" trigger are summarized as follows;

a) A beam particle entered the hydrogen target,

$S1 \cdot S1' \cdot S2 \cdot S2' \cdot$anti's (SHL+SHR+HU+HD+S2 high).

b) An interaction was occured,

anti (BV1·BV2).

c) There were no signals in the anticounters,

anti (TA0+TA1+TA2+TA3+A1+A2+A3).

d) At least two gamma signals above 300 MeV were observed,

N(lead glass groups of main radiator having large signals)>1.

e) Two or three charged particles passed through the spectrometer,

$H0 \cdot (H1>1) \cdot (4>H2>1) \cdot (4>P3Y>1)$.

The logics of "4>P3Y>1" in the last condition was provided by the fast selective trigger (FST) system which will be described in sec. 2–8. The conditions for "N-gamma" events are shown as follows;

f) The conditions of (a), (b), (c) as described as above,
g) No signals from H0, H1 and H2,
h) Sum of the signals from whole lead glass counters exceeded the threshold level of 3 GeV.

2.8 Fast Selective Trigger System

The fast selective trigger system (FST) was used to suppress background triggers. Fig. 13 shows the basic diagarm of FST. Signals of an MWPC (trigger chamber) were fed into a set of trigger logic modules which were called "RAM" modules. Each "RAM" module formed a 64×64 programmable AND logics.

The pattern of the AND logics were preset by the on-line computer. The pulse height of the output signal of the "RAM" module was proportional to the number of coincidence in the preset pattern. The "FST-yes" signal triggered the take-in action of the memory buffer modules described in sec. 2–9. The "FST-no" signal served to clear all the latched data in CAMAC modules. It made the strobed fanout (SFO) module ready and unlocked the inhibited status of CAMAC scalers. The whole decision time for the FST was 800 nsec.

In the present experiment the FST system was used as the multiplicity logic of the y-proportional chamber in W3. Six "RAM" modules were required for 380 anode wires of the chamber. The coincidence pattern of each "RAM" module is also shown in fig. 13. Due to the granularity of coincidence (every 16 wires) the trigger chamber worked as a horizontal hodoscope counter with the width of 3.2 ($=0.2\times16$) cm. The discrimination level was set to select events in which multiplicity of the chamber was two or three. The memory pattern of RAM modules was checked at the beginning and the end of every running cycle. The trigger rate was

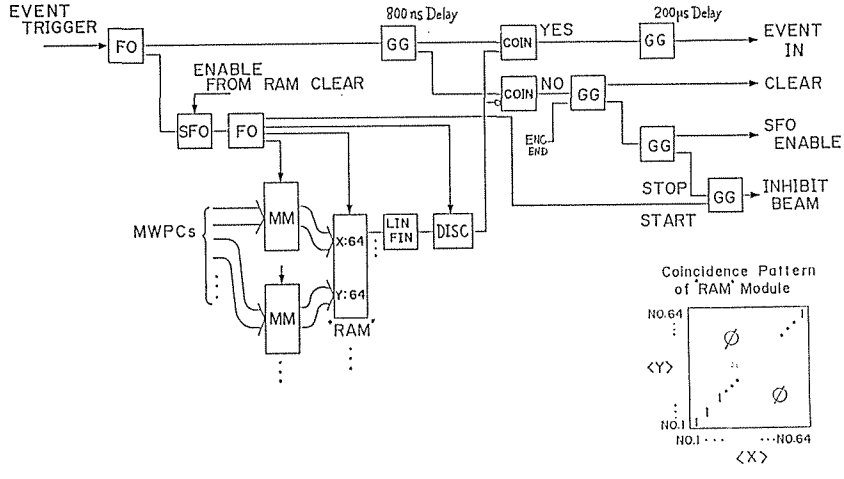

Fig. 13 Basic diagram of FST.

reduced by a factor of 2.5 with the FST system.

The efficiency and multiplicity of the trigger chamber were monitored throughout the experiment to avoid any biases from the FST system. In order to check the FST system, a small sampling data were taken in parallel without being triggered by FST and were written onto magnetic tapes with FST yes-no tag. The same event selection was performed in off-line analysis and the selected events were compared with the events of FST-yes tag. There was no difference between the two selected event groups, and the RAM modules were verified to work accurately.

2.9 Data Acquisition System

The data acquisition and storage were performed on a PDP11/34 computer through CAMAC modules. Each event consisted of hit pattern of MWPC's, timing and amplitude of drift chambers, pulse heights of lead glass counters and other counters. More than 40 events per spill were recorded with a fast and efficient data-taking system (ref. 30). The typical data acquisition time per one event was 200 μsec including the conversion time of TDC and ADC. The data taking rate was finally limited by the buffer memory capacity (32k words) of the on-line computer.

The experimental system was monitored during the data taking. The hit points of the wire chambers and counters plotted on a picture of the experimental setup were displayed on the direct visual on-line monitor. The hit pattern of the wire chambers and counters, and the channel distribution of drift time and pulse height data were also histogrammed at any time. The apparatus was constantly checked by presenting the monitor display on CRT or hard-copy device. The on-line system was connected to the KEK central computer M200H via KEKNET system (ref. 31). The sampled data were sent and analyzed in a M200H computer. The results such as an effective mass spectrum of $\gamma\gamma$ were sent back to the CRT terminal.

The high voltage power supplies for lead glass and scintillation counters as well as FST patterns were controlled and monitored by the on-line computer.

In every running cycle, the detection system was checked by measuring the $\pi^- p$ total cross section. This was done by taking off the signals of all the anticounters except beam anticounters from the trigger logics. The event rate was measured with and without the liquid hydrogen in the target appendix. The typical "full-empty" ratio was 1.51. The measured cross section was about 26 millibarns which is in good agreement with published data.

3. Data Analysis

3.1 Reconstruction Software

The data recorded onto magnetic tapes in 1600 BPI density were analyzed off-line with a HITAC-M200H computer. In the first stage of analysis the data were sorted according to the event number and written to new tapes in 6250 BPI density.

The analysis software was made up of three stages; (i) the track finding for charged particles, (ii) the reconstruction for gamma rays, and (iii) the kinematical analysis. The analysis procedures for charged particles and gamma rays were

described in the following sections. The description of the kinematical analysis will be made in sec. 4–1.

3.1.1 Method of Momentum Reconstruction for Charged Particles

Fig. 14 shows the flow chart of track finding procedure for charged particles. The momentum, direction and position of the incident particles were determined from the information of the beam hodoscope counter BH, and the beam proportional chambers.

At first rough scanning of chamber multiplicity was performed with efficient tracking. The number of hit wires on tracking chambers from W1 to W4 were searched. At least nine chambers among 24 chambers were required to have two to four hit wires.

The track finding process was done independently in x and y projections. The first step was done for the y-projection. In order to carry out the efficient analysis for multi-track events, the hit points of the y-views were sorted into a number of straight sections. The straight sections were formed by connecting the the hit points of the y-proportional chamber in W3 with the target volume. This proportional chamber was used as the trigger chamber for FST system described in sec. 2–8. These sections were required to contain the hit points on at least seven chambers including more than one proportional hcamber. The events with two such straight sections were selected. The final set of hit points in the section were selected by straight line fitting. The y- and z-coordinates of the intersection of the two fitting lines were temporarily regarded as those of the reaction point. The x-coordinate of the reaction point was obtained by extrapolating the incident beam trajectory. The reaction point was required to be roughly within the target region.

The next step was the point selection of the x-chambers. Outside of the analysing magnet the magnetic field was so weak that the hit points of x-chambers in W2 were connected by straight lines with reaction point which was obtained in the y-projection. Searches for good track candidates were made in such a way that at least five out of nine layers of x-chambers in W1 to W3 had hit points around the straight lines.

The fitting line was used to select the hit points of x-chambers in W2, W3 and W4. The above straight line was extrapolated to the magnet center. From this central point, another straight line was drawn to each hit point of W4. The angle between the two straight lines gave the approximate bending angle of the possible trajectory. The magnetic field was approximated to be uniform. The x-positions at W2 and W3 were estimated by a simple calculation of a circular trajectory. The trajectory was selected if the deviation of the hit points of W2, W3 and W4 from the circular curve was within the anode wire spacing of the drift chamber in each chamber set. The information of H1 and H2 as well as that of "two-dimensional" drift chambers was used not only to confirm the track but to resolve the stereo-ambiguity by combining the x- and y-views.

The left-right ambiguity for drift chambers was resolved at each chamber set by using the direction of the approximated trajectory. The final set of x- and y-

coordinates of the hit points for each track candidate was fit by the spline method (ref. 32) and the momentum vector of the charged particle was determined.

The distance between the two tracks was calculated by straight line extrapolation of the tracks to the target region. The reaction point was derived by taking the medium point at the minimum distance between the two tracks. The distance was required to be less than 6 mm and the reaction point was required to be within the target appendix region. The opposite signs for the two charged particles were required.

The position of tracking chambers were carefully adjusted so that the deviation of the actual hit points from the fitted track became minimum. The drift velocity and sense wire position in the TDC count for drift chambers were obtained for each wire by fitting the space-time relationship. These parameters were measured for each running cycle. The efficiency of the chamber was also calculated by off-line analysis and was used to estimate the efficiency of the charged particle tracking with a Monte Carlo simulation.

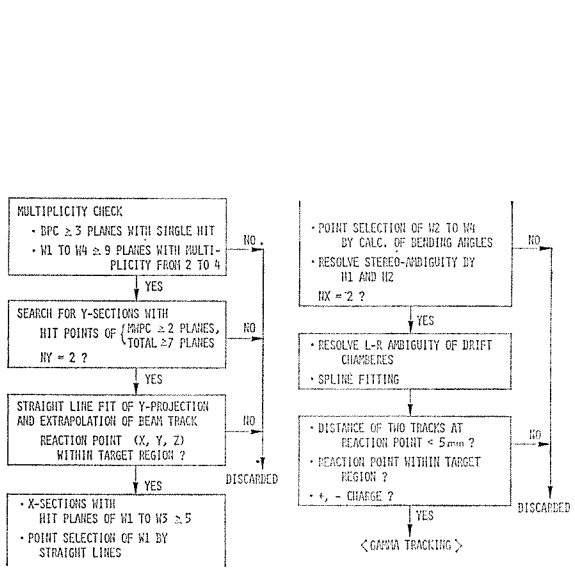

Fig. 14 Flow chart of reconstruction for charged particles. Fig. 15 Flow chart of reconstructionfor gamma rays.

3.1.2 Energy and Position Reconstruction of Gamma Rays

After reconstructing the charged particle tracks, the selected events had two charged particles and a number of possible gamma ray candidates. The flow chart of the reconstruction procedure for gamma rays is shown in fig. 15.

The pulse heights of the lead glass counters from 176 blocks of main radiator array and 28 blocks of active converter array were converted into energy values by subtracting the pedestal values of ADC's and multiplying the energy scale factors. The method to obtain the energy scale factors will be described in sec. 3–2.

The position of gamma ray shower was derived by searching "clusters" of

signaled wires and cathode strips of W5. A cluster was defined by a group of signaled wires (s) or strips (u, v), in which the adjacent signaled ones were located within 15 and 12 times of the spacing of wires and strips, respectively.

The x- and y-coordinates were calculated from the intersection of three groups of wires and strips. If the pulse height of the lead glass block of the main radiator just behind the intersection was large enough, this intersection was regarded as the position of a gamma ray candidate. The energy was derived by summing up the deposit energy in the lead glass block, surrounding blocks and the corresponding active converter.

The positions of the charged particles at W5 were derived by extraporating the charged particle tracks to W5. If the positions of the charged particles at W5 coincided with the position of the gamma ray within 15 cm, the gamma ray candidates were removed. The events with two gamma ray positions apart from that of the charged particles were regarded as the required "2C2G" events.

The reaction point derived from the charged particle reconstruction was used to determine the momentum vector of the gamma rays. Fig. 16 shows the summed momentum spectrum of two charged particles before and after the gamma ray reconstruction. In fig. 16 a large peak around 8 GeV/c corresponds to the reaction $\pi^- p \to \pi^+\pi^- n$. In fig. 16 most of the the $\pi^+\pi^-$ events were eliminated by the removal of the gamma candidates near the charged tracks and by the requirement of NG=2. A small peak of remaining background (about 2.8%) around 8 GeV/c were eliminated by the further cut for $\gamma\gamma$ effective mass.

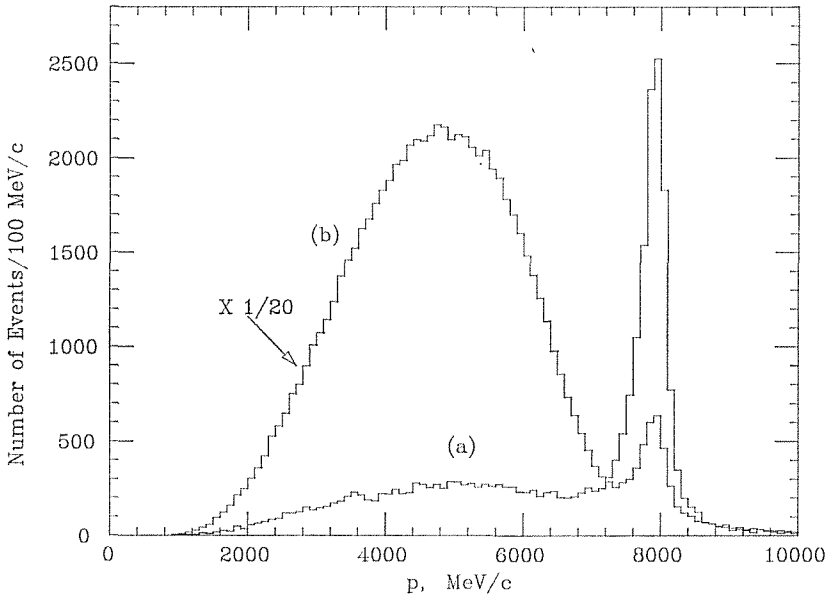

Fig. 16 Summed momentum spectra of two charged particles (a) before and (b) after gamma ray tracking.

3.2 Measurement Accuracy

The deviation of the actual hit point of each chamber from the reconstructed track coordinate was used to estimate the spatial resolution. Fig. 17 shows distribution of the deviation for typical MWPC and typical drift chamber. The average spatial resolution of MWPC's was 2.0 mm (FWHM) reflecting the anode wire spacing. The average spatial resolution of drift chambers was 800 μm (FWHM) reflecting the multiple scattering of the charged particles in chamber materials, the time resolution of TDC and the chamber alignment error. These were the same in x- and y-coordinates.

The charged particle momentum resolution was measured for several beam momenta and amounted to be better than 1.3% over the full momentum range of the charged particles of "2C2G" events. The result of the Monte Carlo estimation substituting the above chamber resolution agrees well with the mesaurement quite well. The momentum resolution $\delta p/p$ can be represented by the following equation,

$$\delta p/p(\%) = \sqrt{(0.58)^2+(0.18p)^2}. \tag{11}$$

Fig. 18 shows the effective mass of $\pi^+\pi^-$ system whose data was taken simultaneously in the regular run by the K^0s trigger mode (table 5). A sharp peak of K^0s shows the mass resolution of 11 MeV (FWHM).

Fig. 19 shows the z-vertex distribution. The distribution between ± 10.5 cm

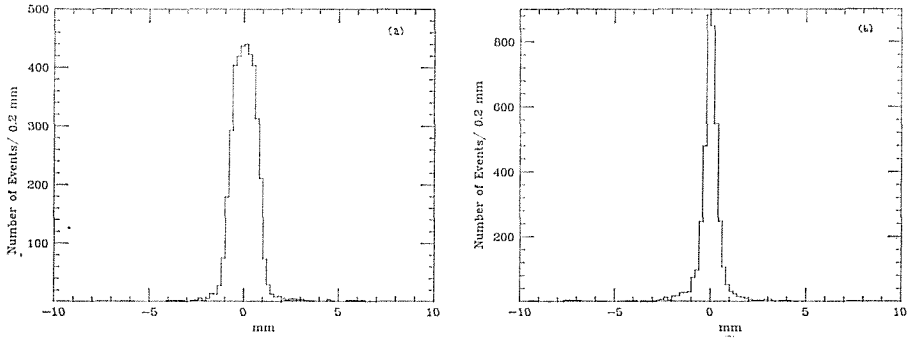

Fig. 17 Deviation of hit points from fitte dtracks in typiacl (a) MWPC and (b) drift chamber.

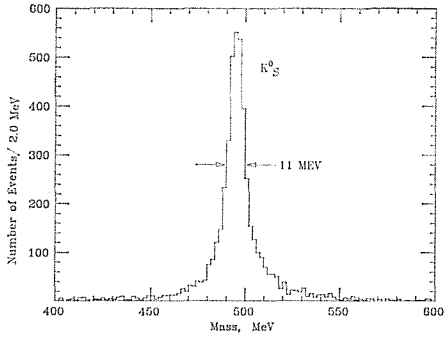

Fig. 18 Effective mass of $\pi^+\pi^-$ in K^0s region.

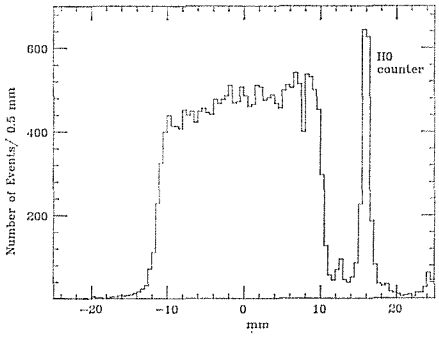

Fig. 19 Reconstructed z-vertex distribution.

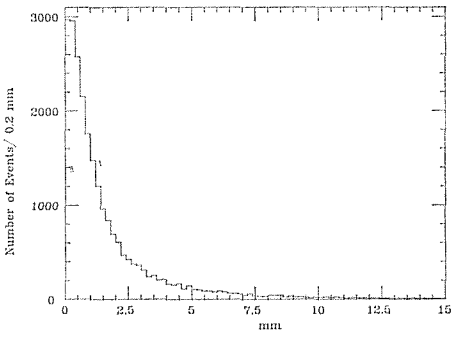

Fig. 20 Distance between two charged particle tracks.

corresponds to the reactions in the hydrogen target. A sharp peak at 16 cm is due to reactions in H0 counter of 2 mm thick. The z-vertex resolution was estimated to be 1.5 cm (FWHM) from the peak width. Fig. 20 shows the distribution of the minimum distance between the reconstructed two charged particle tracks. About 95% of the reconstructed events had the distance within 6 mm. The spatial resolution of the reaction points for x- and y-coordinates was estimated to be 1.0 mm.

The spatial resolution of a gamma ray was measured by the electron beam. The deviation of the shower center from the extraporated electron position in W5 was typically 20 mm (FWHM) for 4 GeV/c electrons and had a little dependence on the momenta from 2 to 4 GeV/c.

The energy scale factors of the lead glass counters were remeasured during the run as follows. About 70% of the main radiator blocks were able to be exposed to the electron beam in position. The electron was identified with a gas Cerenkov counter which was placed between the beam proportional chambers B1 and B2. The rest of main radiator blocks were assumed to have the average energy scale of the measured blocks. The energy scale factors were further refined with "N-gamma" data by the optimization of the effective mass of two gamma rays from η's. The effective mass $M_{\gamma\gamma}$ was calculated for the events of which two γ rays from η hit i'th and j'th main radiator blocks as follows,

$$M_{\gamma\gamma}{}^2 = 4E_iE_j \sin^2(\theta_{ij}/2) \,, \tag{12}$$

where E_i, E_j are energies of the gamma rays measured with the i'th and j'th blocks and θ_{ij} is the angle between the two gamma ray directions. The $\gamma\gamma$ effective mass hisgoram was plotted for all two-gamma events in which i'th block had a large signal. The centroid of the peak in the η region was compared with the mass of η and the energy scale factor of i'th block was corrected by the ratio $\sqrt{M(\eta)/M(\text{centroid})}$. The procedure was applied to all the blocks. The whole procedure was iterated several times.

The energy resolution of gamma rays was estimated as follows. The effective mass M of two gamma rays from neutral pion is given by,

$$M^2 = 2E_1E_2 \cos\theta \,. \tag{13}$$

The energy resolution is related to the $\gamma\gamma$ mass resolution as,

$$\delta M/M = 0.5\sqrt{(\delta E_1/E_1)^2+(\delta E_2/E_2)^2+(\delta\theta\cot(\theta/2))^2}. \quad (14)$$

If we neglect the third term of eq. (14) and select the events of "2C2G" in which $E_1=E_2$, we obtain a simple expression,

$$\delta M/M=(1\sqrt{2})(E/\delta E)\,. \quad (15)$$

The measured energy resolutoin obtained by using the eq. (15) is expressed as follows,

$$\delta E/E(\mathrm{FWHM},\%)=6+13/\sqrt{E}\,. \quad (16)$$

3.3 Corrections due to Detection Efficiencies

In order to obtain the cross sections, the acceptance of the experimental set-up must be estimated with a Monte Carlo simulation program. The acceptance was calculated as a function of the four-momentum transfer squared t', and angles θ and ϕ of the three body ($\pi^+\pi^-\pi^0$ or $\pi^+\pi^-\eta$) decay plane normal vector in the s-channel helicity frame. Here, t' is defined as four momentum transfer squared subtracted by its minimum value $t'=t-t_{\mathrm{min}}$.

In the Monte Carlo simulation program the final states of two-charged and two-gamma events were generated in the Lorentz-invariant phase space. The kinematical variables of the final state praticles were transformed to the laboratory system. The charged particle tracks in the magnetic field were simulated in the Runge-Kutta method. Figs. 21(a), (b) and (c) show the comparison between the Monte Carlo generated data and actual data of "2C2G" events for η and η'. The Monte Carlo results are in good agreement with actula data distributions. The acceptance was estimated as the efficiency where the particles passed through the trigger counters and the defined area of the tracking chambers. Fig. 22 shows the acceptance as a function of t' for η and η'. The area of each chamber was defined narrower than the active area. The same cuts were applied to the actual data as well as Monte Carlo simulated events. The acceptance correction was made on the mesh which segmented the whloe 4π region of $\cos\theta$ and ϕ in 20×20 bins. The acceptance dependence on t' was calculated in 0.1 GeV^2 step and the correction at any t' was made by the interpolation. Figs. 23(a) and (b) show the acceptance-corrected angular distributions of decay plane normal vector in the s-channel helicity frame of η, η' and ω. Flat distributions for η and η' are expected for 0^- particles and the distribution for ω reflects the decay of 1^- particles. To check the stability of acceptance-corrected yield, tighter geometrical cuts (only half of the cnetral part) were applied to both data and simulated events. The cross section increased 5%, 0.8% and 8% for η, ω and η', respectively.

The inefficiencies due to the multiplicity requirements of H1, H2, FST and lead glass counters were estimated as a function of t' with the Monte Carlo simulation. The typical inefficiency was 36%, 25% and 26% for η, ω and η', respectively. The higher inefficiency for η came from the fact that the secondary particles from η was emitted so close that the multiplicity requirements were severe for η due to

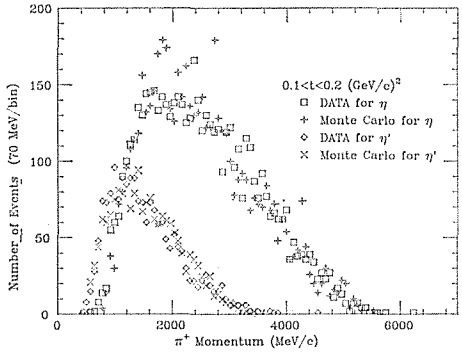

(a)

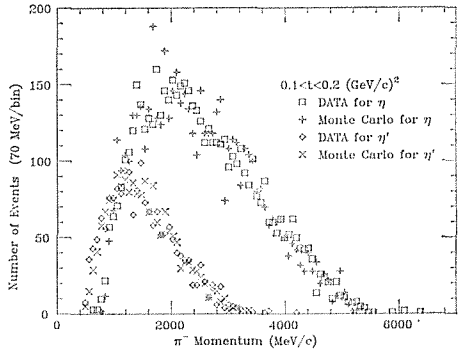

(b)

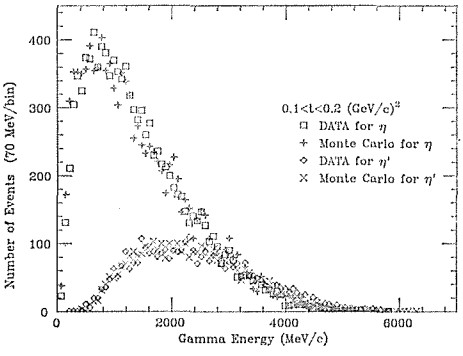

(c)

Fig. 21 Comparison of (a) π^+ and (b) π^- momentum distributions and gamma ray enregy distributins between Monte Carlo and Actual Data of "2C2G" events for η and η'.

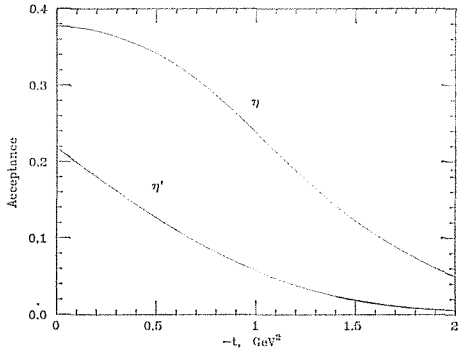

Fig. 22 Geometrical acceptance for η and η' as a function of $-t'$.

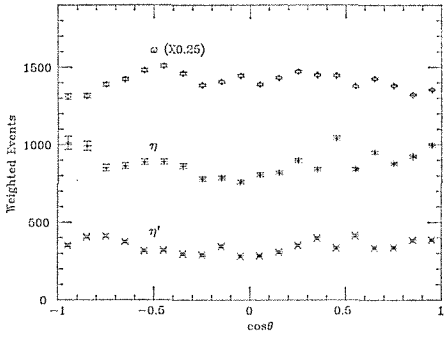

(a)

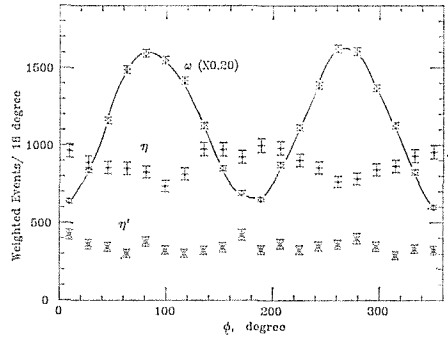

(b)

Fig. 23 Acceptance corrected (a) $\cos\theta$ and (b) ϕ of decay plane normal vector in the s-channel helicity frame of η, η' and ω.

the finite granularity of the trigger counters. Nevertheless our detection efficienny for η seems to be much higher than the previous high statistics experiment (ref. 14), which was able to be drawn a deduction from the comparison of η and η' yields ratio. We detected η three times as much as η' while the experiment of ref. 14, whose acceptance might be comparable with us in η and η' region, only detected 1.9 times η compared to η'. The reason was the finer granularity of lead glass counters compared to ref. 14.

The reconstruction efficiency for charged particles were estimated as follows. From the Monte Carlo events the data for charged particles (the hit address of scintillation counters, wire chambers, TDC counts and pulse height of drift chambers) were generated with the same format as the real data. The generated data were analysed and the number of events passing through the same analysis conditions were examined. The efficiency decreases slowly with $-t'$. The main cause of loss came from the events in which the hit points of the two tracks were too close to separate in x- or y-projections. The fact reflects the lower reconstruction efficiency for η than that for η' or ω.

The effect of the chamber efficiency for the reconstruction failure was estimated by masking a part of the generated hit points of the chambers according to the measured values of the chamber inefficiencies. This estimation was done for each experimental running cycle and for different reactions of $\pi^- p \to \eta n$, $\eta n'$ and ωn. as a function of t'. The average chamber efficiency of typical running cycle was 92.5% and reconstruction efficiencies for charged particles from η, η' and ω at $t'=0$ GeV^2 were 75%, 83%, and 89%, respectively. These values were about 5% lower than those from 100% chamber efficiency.

A correction factor due to the selection critreia that the distance of gamma ray shower and a charged particle at W5 should be greater than 15 cm was carefully examined. The factor had a little dependence with t' and was 0.756 for η, 0.875 for η' and 0.844 for ω.

The detection efficiency for two gamma rays was estimated by the analysis of $\pi^- p \to \eta n$, $\eta \to \gamma\gamma$ events by the following two ways. At first the events were analysed by the data of main radiator only. The events with two showers were selected by the energy deposition pattern on the lead glass array and the mass of two gmama rays was calculated from the deposit energies and roughly estimated positions. The second one was the analysis combined with the information of W5. From the yield ratio of η the detection efficiency was estimated to be 58.0%, which includes the conversion efficiency of two gmama rays (78.0%) in the active converter.

A small amount of data were taken simultaneously with trigger mode of 2C 1 and 2C 2 (table 6) to estimate the rejection rate of good events by target anticounters TA0, TA1, TA2 and TA3. The trigger rate of these data was suppressed by constant factors with count-down logics modules. Fig. 24 shows the beam-normalized distributions of the missing mass squared for two charged particle events (a) with and (b) without the target anticounters, respectively. In fig. 24(b) a shoulder of $\Delta(1232)$ and a broad bump of $\Delta(1650)$ can be seen with the large neutron peak. Fig. 24(a) shows that these background events were rejected by target anticounters.

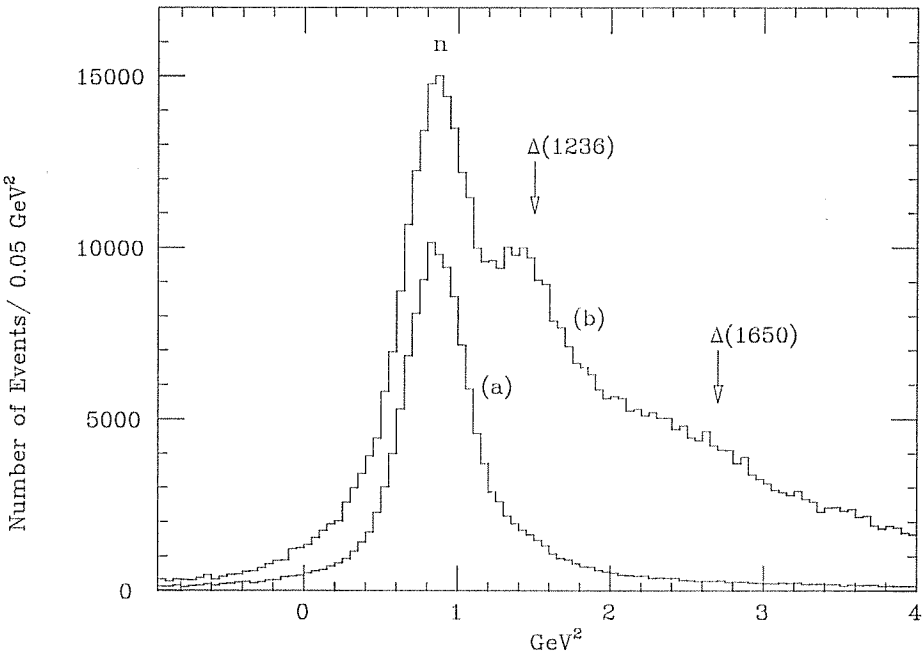

Fig. 24 Missing mass squared distributions (a) with and (b) without target anticounters.

Table 6. Summary of correction factors

<Constant factors>		
1)	Non-conversion of either gamma ray in active converter	0.78
2)	Gamma ray conversion in flight (target, chamber, counter)	0.82
3)	Dead time in data processing	0.94
4)	Inefficiency of beam hodoscope counters and beam proportional chambers	0.97
5)	Accidental veto's by target anticounters (TA0, TA1, TA2, TA3)	0.97
6)	Accidental veto's by anticounters (A1, A2, A3, BV1, BV2)	0.985
7)	Overveto's with target anticounters TA0 by delta-electrons	0.87
8)	Accidental beam tracks	0.97
9)	Tracking efficiency for gamma part	0.744
10)	Reaction of the secondary particles in the target materials	0.975
11)	Overveto's by net neutron detection	0.96
12)	Beam contamination (muons)	0.97
13)	Reactions taking place in the target materials other than liquid hydrogen	0.98
<Corrections estimated by Monte-Carlo simulation>*		
1)	Acceptance of detector system	see fig. 22
2)	Reconstruction efficiency for charged part	0.73 (0.83)
3)	Charged particles and gamma rays within 15 cm at gamma counter	0.76 (0.89)
4)	Ratio of gamma enregy	0.88 (0.96)
6)	Granularity of trigegr counters and chambers	
	H1 and H2	0.65 (0.79)
	Trigger chambers	0.90 (0.93)
	No. of gamma rays	0.99 (1.00)
7)	Decay of π^+ or π^- in flight	0.94 (0.19)

* typical value. ( ) is for η'

The total loss of true events was estimated to be 19.5% by fitting the missing mass distributions in fig. 24 with gaussian functions and taking the ratio of the neutron events. A large part of the event loss (13%) was due to the detection of delta-electrons by TA0. It was estimated from the ratio of TA0 counts to the incident beam particles. Because the rejection ratio by the delta-electrons was proportional to the total length of the charged particles in the target region, the ratio was multiplied by a factor of 1.5 for secondary charged particle production of "2C2G" events. The average event loss due to the neutron detection by target anticounters was reduced to 4% by taking the logial AND of the double layers of TA2. The neutron detection by TA3 was small but it depended on the recoil neutron angle. The Monte Carlo estimation showed that the rejection ratio slowly increases with $-t'$ and it was 3% for η and 6% for η' at $-t'=0.5$ GeV^2. Data was corrected differently for η and η' with the t-dependent factors.

The z-vertex distribution for the empty target showed only 2.3% of the reactions took place from the target materials other than the liquid hydrogen.

A summary of all the correction factors are listed in table 6.

4. Experimental Results

4.1 Procedure for Event Selection

The kinematical variables derived in the reconstruction program were the momenta of the two charged particles, the two gamma rays and the incident particle. They were further analysed to select the good events for reactions (1) and (2). Fig. 25 shows the flow chart of the kinematical analysis.

The detection points of each charged particle and gamma ray were required to be within the defining area of detectors. The momentum cut for each charged particle was set at 400 MeV/c. The cut was slightly higher than the minimum charged particle momentum of 360 MeV/c to pass through the magnet. Each gamma ray was required to have more than the minimum energy of 300 MeV. The ratio of two gamma energies was required to be at least 0.2.

The effective mass spectra of two gamma rays for reactions (1) and (2) are shown in fig. 26. To select the events with two gamma rays decayed from π^0 and η, simple mass cuts of 80 to 200 MeV and 430 to 660 MeV were made as shown by arrows. After the selection with the $\gamma\gamma$ mass cut the energies of the two gamma rays were constrained so that the effective mass became equal to the mass of π^0 or η. The resultant four-vectors of the two charged particles and the constrained four-vectors of the two gamma rays were used to get an effective mass of $\pi^+\pi^-\pi^0$ or $\pi^+\pi^-$.

The distribution of missing mass squared for η and η' region are shown in fig. 27. The clean neutron peaks enabled us to make clear cuts for selecting reactions (1) and (2). The arrows in the figure show the cuts for the missing mass squared which were set between -1.0 and 2.5 GeV^2 for η, and -0.2 and 1.8 GeV^2 for η'. The final four-vector of $\pi^+\pi^-\pi^0$ or $\pi^+\pi^-\eta$ system was given by constraining the recoil nucleon mass to that of neutron.

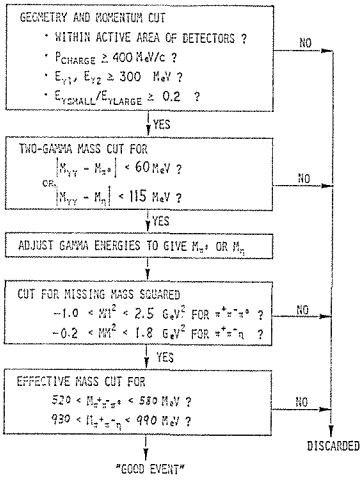

Fig. 25 Flow chart of kinematical anlaysis.

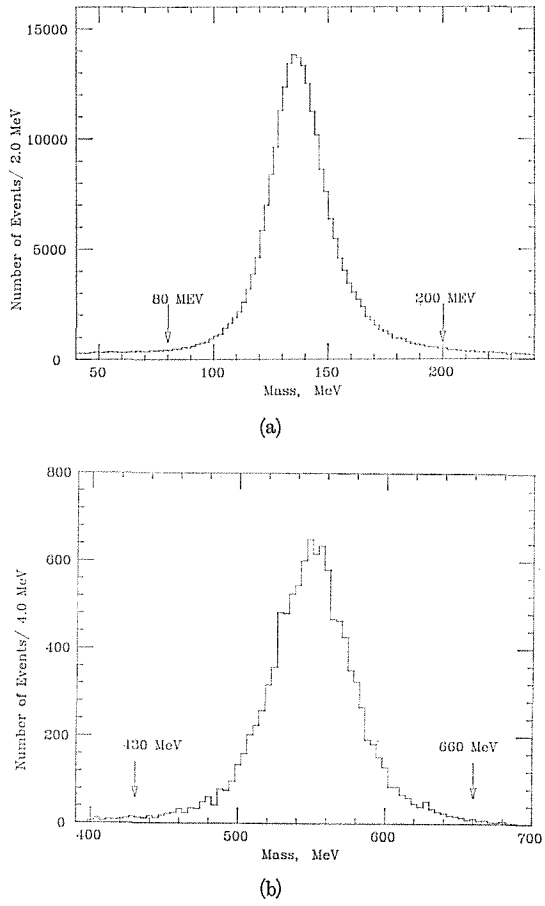

Fig. 26 Effective mass of $\gamma\gamma$ in (a) π^0 and η (b) regions. The $\gamma\gamma$ mass cuts are shown by arrows.

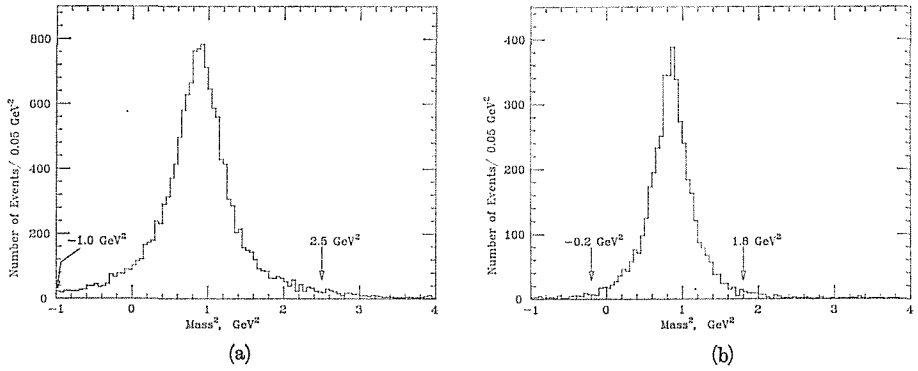

Fig. 27 Missing mass squared of (a) $\pi^+\pi^-\pi^0$ (η region) and (b) $\pi^+\pi^-$ (η' region). The arrows show the missing mass cuts.

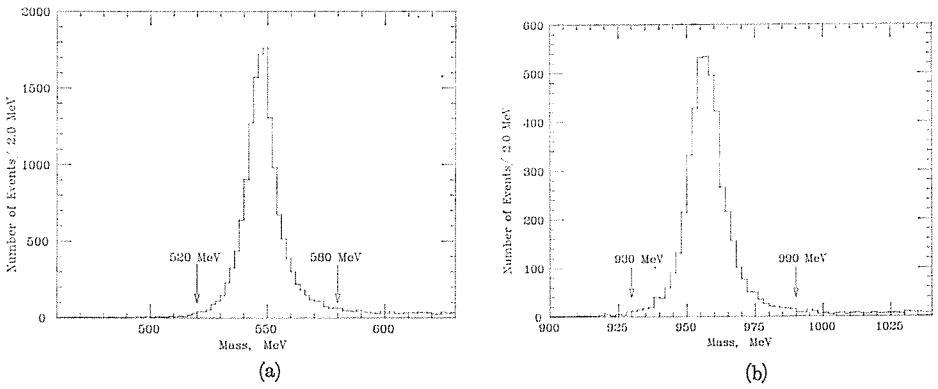

Fig. 28 Effective mass of (a) $\pi^+\pi^-\pi^0$ (η region) and (b) $\pi^+\pi^-\eta$ (η' region). The arrows show the mass cuts.

The effective mass spectra of $\pi^+\pi^-\pi^0$ after the above constraints are shown in fig. 28(a). A clean signal of η is seen with small backgrounds. The effective mass cut of 520 to 580 MeV is shown by arrows. Fig. 28(b) shows the effective mass of $\pi^+\pi^-\eta$. A very clean peak of η' is seen with little backgrounds (less than 3%) between the mass cut of 930 to 990 MeV, which is shown by arrows.

4.2 Cross Sections

The differential cross sections for the reactions (1) and (2) are obtained from experimental data as follows;

$$d\sigma/dt = 1/(C \cdot I \cdot N \cdot \Delta t \cdot B) \cdot \sum_{\theta\phi}(Y(t, \theta, \phi)/A(t, \theta, \phi)) , \tag{17}$$

where,

$Y(t, \theta, \phi)=$ number of good events in a (t, θ, ϕ) bin,
$A(t, \theta, \phi)=$ Acceptance for the (t, θ, ϕ) bin,
$I=$ number of incident beam particles,
$N=$ number of protons in the hydrogen target per unit area,
$\Delta t=$ bin width of the four-momentum transfer squared t,
$C=$ correction factors described in sec. 3–3.
$B=$ branching ratio for decyas of (12) and (13),
[The values of following branching ratios (ref. 33) were used in the corrections for unobserved decay modes,
$(\eta \to \pi^+\pi^-\pi^0)/(\eta \to \text{all}) = 0.237 \pm 0.005$,
$(\eta \to \pi^+\pi^-\eta)/(\eta' \to \text{all}) = (2/3)(0.653 \pm 0.016)$,
$(\eta \to \gamma\gamma)(\eta \to \text{all}) = 0.390 \pm 0.008$.
$\theta, \phi=$ polar and azimuthal angles of three body ($\pi^+\pi^-\pi^0$, $\pi^+\pi^-\eta$) decay plane normal for the reactions (1) and (2) in the s-channel helicity frame.

4.2.1 Total Cross Sections

The differential cross sections for the reactions (1) and (2) measured with this experiment are listed in table 7. By integrating the differential cross sections the

total cross sections σ_T's and the ratio $R(\eta'/\eta)_T$ were obtained as follows,

$$\sigma_T(\pi^- p \to \eta n) = 33.6 \pm 1.5\ \mu\text{b},$$
$$\sigma_T(\pi^- p \to \eta' n) = 16.9 \pm 0.6\ \mu\text{b},$$

and

$$R(\eta'/\eta)_T = 0.50 \pm 0.03.$$

Table 7. Differential cross sections of π^-p$\to\eta$n and π^-p$\to\eta'$n at 8.06 GeBV/c beam momentum

Δt (GeV)^2	t	dσ/d$t(\eta)$(μb)	σd/d$t(\eta')$(μb)	$R(\eta'/\eta)$
0.00–0.02	0.01	50.47±2.17	29.93±2.17	0.59±0.05
0.02–0.04	0.03	68.56±2.56	39.83±2.49	0.58±0.04
0.04–0.06	0.05	78.82±2.78	44.41±2.64	0.56±0.04
0.06–0.08	0.07	89.98±2.98	50.43±2.85	0.56±0.04
0.08–0.10	0.09	81.80±2.87	48.51±2.75	0.59±0.04
0.10–0.12	0.11	93.92±3.13	53.22±3.03	0.57±0.04
0.12–0.14	0.13	91.90±3.12	51.77±2.98	0.56±0.04
0.14–0.16	0.15	87.81±3.06	47.41±2.89	0.54±0.04
0.16–0.18	0.17	88.59±3.16	46.48±2.93	0.52±0.04
0.18–0.20	0.19	81.98±3.06	44.55±2.89	0.54±0.04
0.20–0.22	0.21	75.48±2.98	40.10±2.82	0.53±0.04
0.22–0.24	0.23	74.74±3.00	41.91±2.88	0.56±0.04
0.24–0.26	0.25	69.08±2.93	34.53±2.69	0.50±0.04
0.26–0.28	0.27	69.77±3.02	33.67±2.67	0.48±0.04
0.28–0.30	0.29	64.43±2.92	34.26±2.71	0.53±0.05
0.30–0.32	0.31	62.47±2.95	30.05±2.59	0.48±0.05
0.32–0.34	0.33	53.85±2.78	20.87±2.14	0.39±0.04
0.34–0.36	0.35	56.96±2.93	21.58±2.29	0.38±0.04
0.36–0.38	0.37	53.20±2.89	19.73±2.11	0.37±0.04
0.38–0.40	0.39	47.45±2.75	19.49±2.24	0.41±0.05
0.40–0.45	0.425	40.12±1.65	16.07±1.30	0.40±0.04
0.45–0.50	0.475	33.27±1.51	10.81±1.10	0.32±0.04
0.50–0.55	0.525	25.76±1.35	8.47±1.03	0.34±0.04
0.55–0.60	0.575	22.43±1.30	5.04±0.81	0.22±0.04
0.60–0.65	0.625	16.45±1.13	4.50±0.80	0.27±0.05
0.65–0.70	0.675	13.71±1.05	2.50±0.65	0.18±0.05
0.70–0.80	0.750	7.97±0.58	1.47±0.38	0.18±0.05
0.80–0.90	0.850	5.02±0.49	1.83±0.51	0.37±0.11
0.90–1.00	0.950	2.51±0.35	0.59±0.34	0.24±0.14
1.00–1.20	1.100	1.12±0.17	0.29±0.17	0.26±0.15
1.20–1.40	1.300	0.71±0.16	0.67±0.33	0.94±0.52
1.40–1.60	1.500	0.30±0.12	1.79±0.67*	4.94±2.47**
1.60–1.80	1.700	0.55±0.18		
1.80–2.00	1.900	0.41±0.21	1.37±1.37**	3.08±3.42**

* Δt=1.4−1.7
** Δt=1.7−2.6

The errors include the systematic errors due to the uncertainties in the correction factors listed in table 6 and the background substractions (4.5% for η and 3.3% for η').

The values of the total cross sections for η and η' are shown in fig. 29 together with the results of the previous experiments (refs. 3, 4, 5, 8, 10, 11, 12 and 14 for η and refs. 5, 7, 9, 13 and 14 for η'). From the present ratio of the total cross sections eq. (9) leads to the octet-singlet mixing angle of $-(19.4\pm0.8)°$, as is shown in table 8. Our result is consistent with ref. 13 and is different from the result of ref. 14. Our result of 0.50 ± 0.03 for $R(\eta'/\eta)_T$ ($-19.4°$ for the mixing angle) clearly deviates from 0.35 ($-24°$) expected from the simple SU(3) model.

The energy dependence of the cross sections can be described by the power-law function,

Table 8. Shaping parameters. Cross sections and ratio for η and η'.
$d\sigma/dt=(A-Bt)\exp(ct)=A(1-gct)\exp(ct)$

	Apel et al. (refs. 12 and 13) 25 GeV/c	Apel et al. (refs. 12 and 13) 40 GeV/c	Stanton et al. (ref. 14) 8.45 GeV/c	This experiment 8.06 GeV/c
$<\eta>$				
A (μb·GeV^{-2})	13.6 ± 0.51	7.7 ± 0.33	44.4 ± 4.8	48.9 ± 1.7
B (μb·GeV^{-4})	423 ± 28	262 ± 18	1405 ± 75	986.4 ± 15.2
c (GeV^{-2})	8.4 ± 0.1	9.2 ± 0.1	6.82 ± 0.12	5.99 ± 0.03
g	3.7 ± 0.2	3.7 ± 0.2	4.63 ± 0.56	3.37 ± 0.13
$<\eta'>$				
A (μb·GeV^{-2})	7.37 ± 1.16	4.89 ± 0.581	21.2 ± 2.8	26.98 ± 1.82
B (μb·GeV^{-4})	312 ± 98	76 ± 42	920 ± 60	726.7 ± 20.0
c (GeV^{-2})	9.4 ± 0.5	10.3 ± 0.5	8.69 ± 0.18	7.55 ± 0.06
g	4.5 ± 1.2	3.5 ± 0.7	4.99 ± 0.742	3.57 ± 0.55
$\sigma_T(\eta)$ (μb)	7.68 ± 0.39	4.03 ± 0.18	36.4 ± 3.6	33.6 ± 1.5
$\sigma_T(\eta')$ (μb)	4.05 ± 0.30	2.10 ± 0.15	14.6 ± 1.4	16.9 ± 0.6
$R(\eta'/\eta)_T$ and mixing angle θ (degree)	0.52 ± 0.03	0.52 ± 0.02	0.401 ± 0.03	
	-18.9 ± 0.78	-18.9 ± 0.52	-22.4 ± 0.97	-19.4 ± 0.8
$R(\eta'/\eta)$ at $t=0$ and mixing angle θ (degree)	0.50 ± 0.08	0.59 ± 0.07	0.48 ± 0.09	0.552 ± 0.04
	-19.5 ± 2.16	-17.2 ± 1.64	-20.1 ± 2.25	-18.1 ± 1.04

$$\sigma_T = C_1\left(\frac{s}{s_0}\right)^{-C_2}\mu\text{b} . \tag{18}$$

where s is the square of the energy in the center-of-mass system, and s_0 is 10 GeV^2. By fitting our results and those of ref. 11, the values of C_1 and C_2 for η are evaluated to be

$$C_1(\eta) = 70.1\pm3.29 \quad C_2(\eta) = 1.49\pm0.02 .$$

For η', the fit of our results and those of ref. 13 leads to

$$C_1(\eta') = 31.5\pm1.58 \quad C_2(\eta') = 1.29\pm0.04 .$$

As shown in fig. 29, both of the solid lines with these parameters reproduce well the other data in the wide beam momentum region. The value of $C_2(\eta')$ is 13% smaller than $C_2(\eta)$. Apel et al. (ref. 13) obtained about the same values for $C_2(\eta')$ and $C_2(\eta)$ by fitting only their data of 15 to 40 GeV/c beam momenta. However, their $C_2(\eta')$ does not seem to describe well the cross sections at other momenta.

Our larger value of $C_2(\eta)$ than that of $C_2(\eta')$ indicates that the total cross section of η decreases faster than that of η' and that the total cross sections of η and η' will become equal to each other at the incident momentum of about 300 GeV/c.

4.2.2 Differential Cross Sections

The differential cross sections for the reactions (1) and (2) are shown in fig. 30. The solid and dotted lines are the fits by the phenomenological formula given below. The differential cross sections of η and η' have a similar shape in the $|t|<0.8$ GeV^2 region. They show a marked drop at small $|t|$ and smooth falloff for $|t|$ beyond 0.1 GeV^2.

In the $|t|<0.8$ GeV^2 region the differential cross sections can be described well by the phenomenological formula (refs. 8 and 12) which is the sum of the absolute square of the neutron spin-flip and spin-nonflip amplitudes,

$$\mathrm{d}\sigma/\mathrm{d}t = A(1-gct)\exp(ct) , \tag{19}$$

where the parameters mean as follows;

- A : the value of $\mathrm{d}\sigma/\mathrm{d}t$ at $t=0$, or the absolute square of spin nonflip amplitude at $t=0$.
- g : the ratio of the integrated cross sections for spin flip and nonflip.
- c : the exponential slope parameter.

The assumption that the slope parameters for spin-flip and spin-nonflip amplitudes are equal was verified by the analysis of the reaction (1) (ref. 12). The parameters which were derived by the least-squares fitting for $|t|<0.8$ GeV^2 region are also listed in table 8.

In the larger momentum transfer region ($|t|>1.0$ GeV^2) a dip or change of the slope is seen in both differential cross sections. However, the behavior of the differential cross sections for η and η' in this t region is different each other.

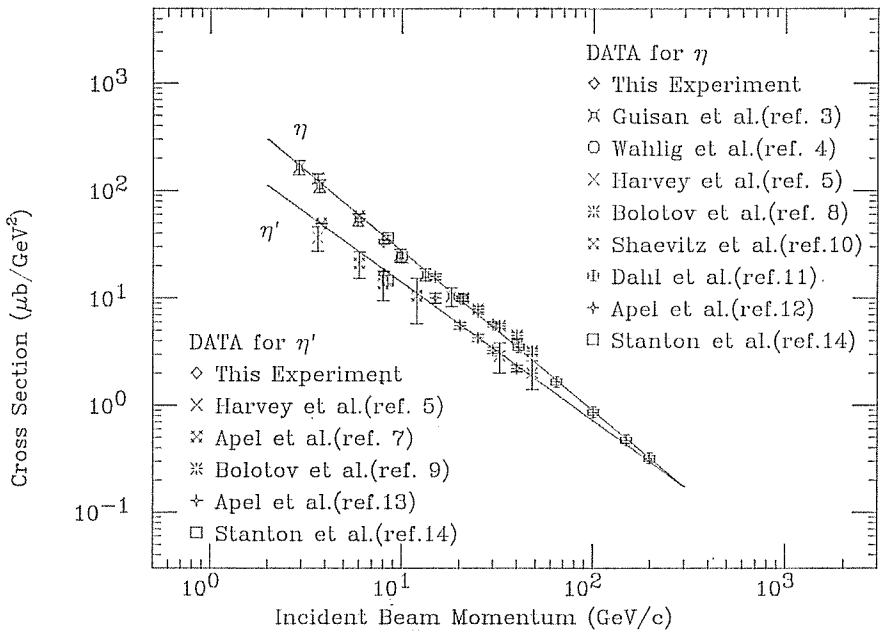

Fig. 29 Total cross sections of $\pi^- p \to \eta n$ and $\eta' n$. The solid lines are the power-law function (eq. 18) fit to our results and those of previous experiments described in the text.

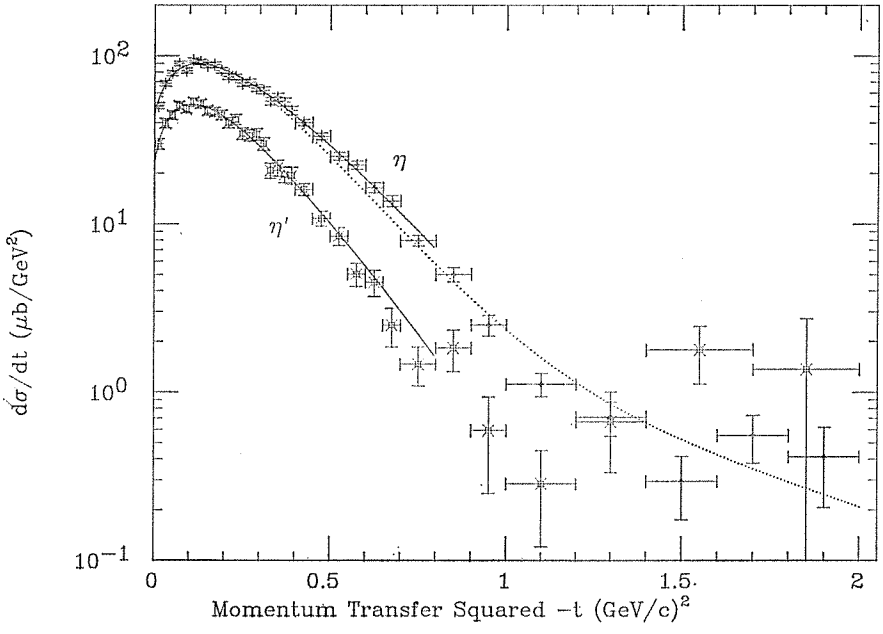

Fig. 30 Differential cross secio sections of $\pi^- p \to \eta n$ and $\eta' n$ at 8.06 GeV/c. The solid lines are the fit by the formula (eq. 19) for $|t| < 0.8$ GeV^2 region. The dotted line is the fit by the Regge+Cut model (Ref. 35).

The differential cross sections of η falls much more slowly than in the smaller $|t|$ region. While, the differential cross sections of η' shows an increase in this t region.

The ratio of the differential cross sections, $R(\eta'/\eta)$, is shown in fig. 31 together with those of refs. 13 and 14. Our data shows a clear t-dependence of $R(\eta'/\eta)$ over the measured t region. $R(\eta'/\eta)$ decreases by a factor of 3 in the $|t|<0.8$ GeV^2 region. Beyond $|t|=1$ GeV^2, $R(\eta'/\eta)$ increases and reaches to 1.0 around $|t|=$ 1.3 GeV^2. The value of $R(\eta')$ at $t=0$ is 0.55 ± 0.04. Using eq. (9) we obtain the $\eta-\eta'$ mixing angle of $-(18.1\pm1.04)°$ as is listed in table 8. Again our mixing angle is different from ones obtained from the SU(3) mass formula.

Compared with other experiments, clear decrease of $R(\eta'/\eta)$ of our data is consistent with Stanton et al. (ref. 14). However, their values which are restricted in $|t|<0.8$ GeV^2 region are about 10 to 20% smaller than ours. Apel et al. (ref.

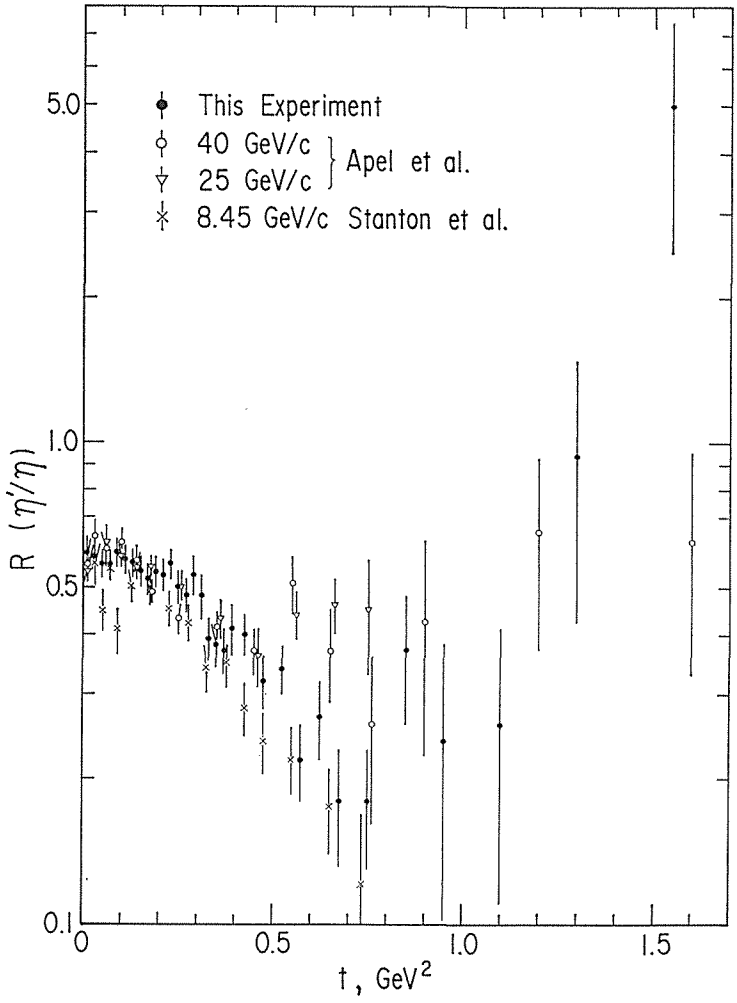

Fig. 31 Ratios of differential cross sections of this experiment and refs. 13 and 14.

13) who obtained data using a neutral spectrometer insisted that $R(\eta'/\eta)$ did not depend on t. But it seems that $R(\eta'/\eta)$ of their data also decreases from 0.6 to 0.26 in $|t|<0.8$ GeV^2. Their values are in agreement with ours at $|t|<0.5$ GeV^2, but around $|t|=0.7$ GeV^2 they are higher than ours. The increase of $R(\eta'/\eta)$ in the large $|t|(>1.0$ GeV^2) region is observed in our data. This behavior is not clear in the result of the previous experiments (ref. 13). However, in the $|t|$ region of 0.8 to 1.3 GeV^2 their values are in agreement with ours.

As for the small $|t|$ region (<0.8 GeV^2), the least-squares fit of the differential cross sections with eq. (19) was made, and in fig. 32, the shape parameters c, A and g for η and η' of our experiment are shown together with those of the previous experiments as a function of the incident momentum. The s dependences of the shape parameters defined by eq. (19) are evaluated by fitting the data of this experiment and those of refs. 3, 10, 11, 13 and 14 for η and refs. 13 and 14 for η'. The results are as follows;

$$c(\eta) = 5.73+1.761 \ln (s/s_0) , \tag{20}$$

$$c(\eta') = 7.41+1.41 \ln (s/s_0) , \tag{21}$$

$$A(\eta) = 86.2\left(\frac{s}{s_0}\right)^{-1.21} , \tag{22}$$

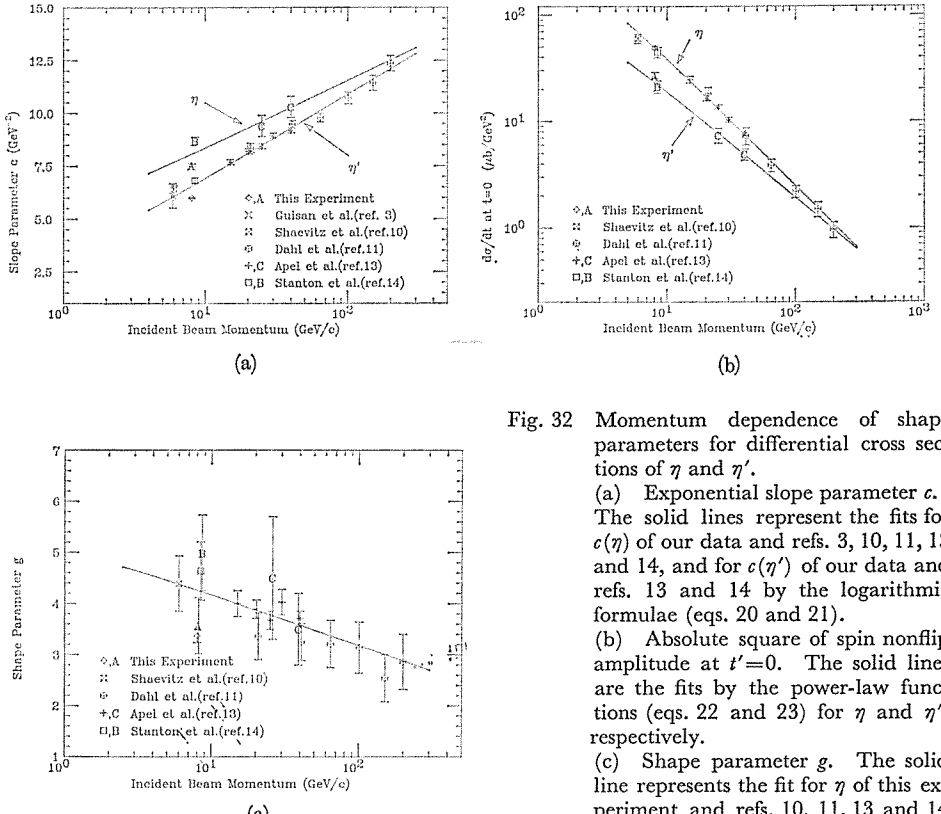

Fig. 32 Momentum dependence of shape parameters for differential cross sections of η and η'.
(a) Exponential slope parameter c. The solid lines represent the fits for $c(\eta)$ of our data and refs. 3, 10, 11, 13 and 14, and for $c(\eta')$ of our data and refs. 13 and 14 by the logarithmic formulae (eqs. 20 and 21).
(b) Absolute square of spin nonflip amplitude at $t'=0$. The solid lines are the fits by the power-law functions (eqs. 22 and 23) for η and η', respectively.
(c) Shape parameter g. The solid line represents the fit for η of this experiment and refs. 10, 11, 13 and 14 by the logarithmic function (eq. 24).

$$A(\eta') = 37.0\left(\frac{s}{s_0}\right)^{-1.01}, \tag{23}$$

$$g = 4.46 - 0.44 \ln (s/s_0) . \tag{24}$$

It seems that at sufficient high momentum around 300 GeV/c, $c(\eta)$ and $A(\eta)$ become equal to $c(\eta')$ and $A(\eta')$, respectively. If we take the ratio of the absolute squares of the nonflip and flip amplitudes at $t=0$ i.e. $R_{nf}=(p/p')A(\eta')/A(\eta)$ and $R_f=(p/p')(A(\eta')c(\eta')g(\eta')/(A(\eta)c(\eta)g(\eta))$, we obtain the R_{nf} and R_f of 0.579 and 0.773, respectively. Here, p/p' is the ratio of the center-of-mass momenta of η and η' for kinematical correction and is 1.05 at 8.06 GeV/c. The large contribution of the spin flip amplitude indicates that R_f is the better quantity for quark content. Again, the value of R_f is different from 0.35 or 0.96 expected from the linear and quadratic mass formulae of SU(3) classification.

4.3 Discussion

The summary of our experimental results are as follows;

1) The total cross sections of η and η' are $33.6\pm1.5\,\mu$b and $16.9\pm0.6\,\mu$b, respectively. The values are consistent with other previous results under the power-law function given by eq. (18).

2) The ratio of the total cross sections for η and η' is 0.50 ± 0.03 and eq. (9) leads to the octet-singlet mixing angle of $(-19.4\pm0.8)°$.

3) The shape of the differential cross sections of η and η' can be well fitted by the phenomenological formula of eq. (19) the four momentum transfer region of $|t|<0.8$ GeV^2.

4) The strong t dependence is seen on $R(\eta'/\eta)$ from our results and can not be explained by the simple SU(3) model.

5) In the region of $|t|<0.8$ GeV^2, the slope parameter of the differential cross sections of η' is 1.2 times greater than that of η, which leads to the decrease of the ratio $R(\eta'/\eta)$ by a factor of 3.1 in this t region.

6) At $t=0$, $R(\eta'/\eta)$ is 0.55 ± 0.04 and from eq. (9) we obtain the octet-singlet mixing angle $(-18.1\pm1.04)°$ of the pseudoscalar nonet.

7) The behavior of the differential cross sections of η and η' changes at around $|t|=1.0$ GeV^2.

8) Beyond 1.0 GeV^2, differential cross sections of η decreases more slowly, whereas those of η' increases with $|t|$ and this brings up the value of $R(\eta'/\eta)$ above 1.

9) Comparing with other experiments, the s-dependence of cross sections are summarized as follows. Both of $\sigma_T(\eta)$ and $\sigma_T(\eta')$ decrease with s, but $\sigma_T(\eta)$ decreases faster than $\sigma_T(\eta')$ and $R(\eta'/\eta)$ increases 27% in the momentum range of 8 to 40 GeV/c. As for the differential cross sections, the shape parameters c and A for η and η' have a clear s-dependence, and the values of c's and A's come close to each other as s increases.

The ratio of the total cross sections and that of the differential cross sections at $t=0$ is about 0.5. However, it is different from both values of $R(\eta'/\eta)=0.96$ or $R(\eta'/\eta)=0.35$ which corresponds to the mixing angles of $-10°$ or $-24°$ expected

from the quadratic and linear mass formulae of the naive SU(3) classification. Okubo and Jagannathan (ref. 34) tested the quark-line rule for reactions involving η and η' and suggested the validity of the general particle-mixing model (ref. 35) based on the topological expansion (ref. 36) for Regge dynamics. With the genreal particle-mixing model Inami et al. derived the different mixing angles of $\theta_2=-6°$ and $\theta_2=-20°$. The model explains $\Gamma(\eta\to\gamma\gamma)$ and $\Gamma(\eta'\to\gamma\gamma)$ and the sum rule for charge exchange reactions from the experimental value of $R(\eta'/\eta)=0.52$. Another phenomenological model (ref. 37), which introduces the violation of OZI rule by mixing matrix of quark wave functions based on QCD, gave the different mixing angles of θ_1 and θ_2 in eq. (7). According to this model θ_1 and θ_2 are $-17.2°$ and $-20.6°$, respectively and $R(\eta'/\eta)=0.53$, which is close to the experimental values.

Cohen and Lipkin proposed a phenomenological model (ref. 16) in which $\eta-\eta'$ mixing are extended to include radial esxcitations in the mass matrix. They obtained $R=3$ and this result can not explain our results.

The strong t-dependence of $R(\eta'/\eta)$ confirmed by the present experiment indicates that the production process of η and η' cannot be explained by the simple model based on the quark line rule which assumes the exact OZI rule.

The fact of exponential decrease of the differential cross sections of η and η', and the larger slope parameter of η' than that of η show that the interaction radius of η' is about 10% larger than that of η, if we assume that the interaction radius is proportional to the squrae root of the slope parameter.

Recentely Saleem and Aleem (ref. 38) showed that the behavior of differential cross sections of η and η' beyond $|t|=1.0$ GeV^2 can be reproduced by using a single Regge pole+cut model. They assumed that $A_2\times P$ cut contributes only to the helicity flip amplitude and that the ratio $R(\eta'/\eta)$ is equal to 0.5 and fitted the data of ref. 12. They showed that the differential cross sections of η' can be reproduced with the same parameters as η. By multiplying their residue functions by a factor of 0.9, our differential cross sections of η can be well fitted over the measured t region as is shown in fig. 30. However this model can not reproduce our differential cross sections of η', because of their asumption of $R(\eta'/\eta)$ which is independent of t.

The study of η and η' mesons produced by the $\pi^- p$ charge exchange reaction has been very effective to obtain the new knowledge of the isoscalar members of the pseudoscalar nonet. However, our knowledge of the pseudoscalar mesons is yet incomplete. As to the total cross section σ_T and the shape parameters A and c of the differential cross sections for η and η', the suggseted asymptotic behavior in which these physical quantities will become equal between η and η' at high energy (around 300 GeV/c) is eager to be tested by the future high energy experiment. In addition high statistics data of η and η' production at high $|t|$ region is needed to obtain further knowledge of the reaction mechanism of the isoscalar mesons.

Acknowledgements

I would like to express my thanks to Prof. K. Takamatsu, Dr. T. Tsuru, Dr. T.

Inagaki and Prof. T. Sato of KEK who gave me both guidance and help with all aspects of the experiment. I would also like to express my great appreciation to the members of our collaboration: Prof. T. Nakamura, Drs. N. Tamura, K. Imai, Y. Inagaki of Kyoto University and Dr. A. Itano of National Institute of Radiogical Sciences, Mr. R. Takashima of Kyoto University of Education and Mr. K. Ohmi of Tsukuba University. My thanks also go to Prof. A. Murakami and Dr. S. Kobayashi of Saga University, Prof. H. Okuno and Dr. K. Maruyama of Institute of Nuclear Science of Tokyo University, Prof. A. Sasaki of Akita University, Dr. A. Ando, Dr. S. Inaba and Mr. Y. Yasu of KEK who gave continuous help during the construction and data taking stage of the experiment.

Special thanks also go to my physics advisor Prof. K. Miyake of Kyoto University who has encouraged me throughout the experiment.

I would especially like to give my special gratitude to Professors of KEK for their great support to this experiment; T. Nishikawa (director), S. Suwa, S. Ozaki, A. Kusumegi, H. Hirabayashi, H. Sugawara and K. Takahashi.

My thanks also go to all the staff in KEK who have made continuous efforts in excellent machine and beam operation, development of electronics, engineering work and computer service. This experiment would not have been possible without their great contribution.

References

1) G. Alexander, H.J. Lipkin and F. Sheck, Phys. Rev. Lett. **17** (1966) 412.
2) N.M. Kroll, T.D. Lee, and B. Zumino, Phys. Rev. **157** (1967) 1376.
3) O. Guisan et al., Phys. Rev. Lett. **18** (1965) 200.
4) M. Wahlig and I. Mannelli, Phys. Rev. **168** (1968) 1515.
5) E.H. Harvey et al., Phys. Rev. Lett., **27** (1971) 885.
6) W.D. Apel et al., Phys. Lett., **40B** (1972) 680.
7) W.D. Aple et al., Phys. Lett., **46B** (1973) 459.
8) V.N. Bolotov et al., Nucl. Phys. **B73** (1974) 387.
9) V.N. Bolotov et al., Phys. Lett. **48B** (1974) 280.
10) Shaevitz et al., Phys. Rev. Lett. **36** (1976) 5.
11) O.I. Dahl et al., Phys. Rev. Lett. **37** (1976) 80.
12) W.D. Apel et al., Nucl . Phys. **B152** (1979) 1.
13) W.D. Apel et al., Phys. Lett. **83B** (1979) 131.
14) N.R. Stanton et al., Phys. Lett. **92B** (1980) 353.
15) H.J. Lipkin, Phys. Lett., **67B** (1977) 65.
16) I. Cohen and H.J. Lipkin, Nucl. Phys. **B151** (1979) 16.
17) N.H. Fuchs, Phys. Rev. **D14** (1976) 1912.
18) R.H. Capps, Phys. Rev. **D17** (1977) 1862.
19) T. Inagaki et al., Cryogenic Engineering, **vol. 18**, No. 16 (1983) 296.
20) F. Sauli, CERN **77–09**, 3 May 1977.
21) M. Breidenbach, F. Sauli and R. Tirler, Nucl. Instr. and Meth. **108** (1973) 23.
22) A. Breskin et al., Nucl. Instr. and Meth. **119** (1974) 9.
23) B. Sadoulet and A. Litke, Nucl. Instr. and Meth. **124** (1975) 349.
24) A. Breskin et al., Nucl. Instr. and Meth. **124** (1975) 189.
25) Y. Suzuki, Memoirs of the Fuculty of Science, Kyoto University, Series of Physics, Astrophysics, Geophysics and Chemistry, **37** (1981) 73.
26) M. Minowa, Memoirs of the Fuculty of Science, Kyoto University, Series of Physics, Astrophysics, Geophysics and Chemistry, **37** (1981) 109.

The authour would like to express special thanks to CEX group for providing the lead glass counters.

27) R.L. Ford and W.R. Nelson, **SLAC–210, UC–32,** June 1978.
28) A. Ando et al., **KEK–79–21.**
29) M. Kobayashi et al., Nucl. Instr. and Meth. **224** (1984) 318.
30) M. Ikeno et al., Nucl. Instr. and Meth. **225** (1984) 347.
31) Y. Asano et al., Nucl. Instr. and Meth. **159** (1979) 7.
32) H. Wind, Nucl. Instr. and Meth. **115** (1974) 431.
33) Rev. of Mod. Phys. **Vol. 56,** No. 2, Part II April 1984.
34) S. Okubo and K. Jagannathan, Phys. Rev. **D 15** (1977) 177.
35) T. Inami et al., Phys. Lett. **61B** (1976) 60.
36) G. Veneziano, Phys. Lett. **52B** (1974) 220.
37) A.T. Filippov, Yad. Fiz. **29,** 1035 (April 1979).
38) M. Saleem and F. Aleem, Phys. Rev. **D 24** (1981) 2403.